*Cardiovascular Engineering and Technology*, Vol. 4, No. 4, December 2013 *(© 2013)* pp. 440–463
DOI: 10.1007/s13239-013-0151-9



# Numerical Comparison and Calibration of Geometrical Multiscale Models for the Simulation of Arterial Flows

A. CRISTIANO I. MALOSSI[1] and JEAN BONNEMAIN[1,2]

[1]MATHICSE, Mathematics Institute of Computational Science and Engineering, EPFL, École Polytechnique Fédérale de Lausanne, Station 8, 1015 Lausanne, Switzerland; and [2]CHUV, Centre Hospitalier Universitaire Vaudois, Rue du Bugnon 21, 1011 Lausanne, Switzerland

*(Received 15 November 2012; accepted 7 May 2013; published online 1 June 2013)*

Associate Editor Ajit P. Yoganathan oversaw the review of this article.

**Abstract**—Arterial tree hemodynamics can be simulated by means of several models of different level of complexity, depending on the outputs of interest and the desired degree of accuracy. In this work, several numerical comparisons of geometrical multiscale models are presented with the aim of evaluating the benefits of such complex dimensionally-heterogeneous models compared to other simplified simulations. More precisely, we present flow rate and pressure wave form comparisons between three-dimensional patient-specific geometries implicitly coupled with one-dimensional arterial tree networks and (i) a full one-dimensional arterial tree model and (ii) stand-alone three-dimensional fluid–structure interaction models with boundary data taken from precomputed full one-dimensional network simulations. On a slightly different context, we also focus on the set up and calibration of cardiovascular simulations. In particular, we perform sensitivity analyses of the main quantities of interest (flow rate, pressure, and solid wall displacement) with respect to the parameters accounting for the elastic and viscoelastic responses of the tissues surrounding the external wall of the arteries. Finally, we also compare the results of geometrical multiscale models in which the boundary solid rings of the three-dimensional geometries are fixed, with respect to those where the boundary interfaces are scaled to enforce the continuity of the vessels size with the surrounding one-dimensional arteries.

**Keywords**—Geometrical multiscale modeling, Blood flow models, Fluid–structure interaction, Wave propagation, Patient-specific geometries, Aorta and iliac arteries.

## INTRODUCTION

Numerical simulations based on complex mathematical approaches have become an effective tool to model arterial flow dynamics. Research in this field is essential in order to understand, predict, and treat common and potentially fatal cardiovascular pathologies, such as aneurysms formation, atherosclerosis, and congenital defects, as well as the planning of surgical intervention, usually called predictive surgery.

Thanks to modern supercomputing facilities, modeling big portions of the systemic arterial tree with a fully detailed three-dimensional (3-D) description is nowadays feasible.[48] Nevertheless, the amount of data required by these simulations can be hardly retrieved. Moreover, a compromise between model complexity and computational cost might be still relevant in a medical environment, where huge number of patients need to be assisted at the same time. In this sense, geometrical multiscale approaches provide an efficient and reliable way to select the desired level of complexity in each component of the cardiovascular system.[6,21,37,40,41,47] The main ingredients of a geometrical multiscale model for cardiovascular flows are (i) 3-D fluid–structure interaction (FSI) models, which are used to represent few specific components of main interest,[4,10,13,18,23,25,26,46] (ii) one-dimensional (1-D) FSI models, which describe the global blood circulation in the arterial network,[1,7,8,20,35] and (iii) lumped parameters models, which account for the cumulative effects of all distal vessels, i.e., small arteries, arterioles, and capillaries.[22,45] More generally, from the medical point of view, a 3-D model allows to have a deep insight of a specific region of the cardiovascular system (e.g., the thoracic aorta), whereas the interaction with the global cardiovascular system is modeled by the

Address correspondence to A. Cristiano I. Malossi, MATHICSE, Mathematics Institute of Computational Science and Engineering, EPFL, École Polytechnique Fédérale de Lausanne, Station 8, 1015 Lausanne, Switzerland. Electronic mail: cristiano.malossi@epfl.ch

mean of simpler models obtained through a dimensional reduction.

Despite the fact that the geometrical multiscale modeling technique is widely accepted in the literature, so far the greatest part of the studies has focused mainly on mathematical and methodological aspects. In particular, at the best of our knowledge, there are no studies performing a quantitative comparison between large heterogeneous cardiovascular networks (including at the same time 3-D FSI, 1-D FSI, and lumped parameters models), vs. simplified problems, e.g., stand-alone 3-D FSI simulations or full 1-D FSI problems. Moreover, most of the patient-specific cardiovascular applications in the literature does not make use of networks of 1-D arteries to account for the systemic circulation, which is generally condensed by using lumped parameters models directly coupled with the inlets/outlets of the 3-D geometries of the patients (see, e.g., Balossino *et al.*,[2] Laganàà *et al.*,[30] Baretta *et al.*,[3] and Moireau *et al.*[39]). This is a quite severe modeling assumption, since the flow in the systemic arteries is strongly space-time dependent, thus requiring at least a 1-D axial description of the traveling waves.

To fill this gap, in this work we provide several numerical comparisons of geometrical multiscale models with the aim of proving, and somehow quantifying, the benefits of such complex dimensionally-heterogeneous problems with respect to other simpler approaches. The geometrical multiscale models are set up by coupling one or more 3-D patient-specific geometries with a full network of 1-D models representing the global circulation of an average healthy patient. In particular, since the analysis of pathological scenarios is not considered here, we select two healthy 3-D geometries corresponding to the aorta and the iliac arteries. The results of these models are compared with both a full 1-D network of arteries and stand-alone 3-D FSI simulations, where the data for the latter at the inlet and outlet boundary interfaces are taken from a precomputed full 1-D network simulation. The comparisons are performed mainly in terms of flow rate and pressure waveforms. In addition, we also analyze the 3-D solid wall displacement magnitude.

On a slightly different context, we also focus on the calibration of cardiovascular simulations. Indeed, a key aspect to consider in order to obtain results in the physiological range is the tuning of the problem parameters, especially for modeling 3-D FSI arteries. In the literature there are several works on parameter estimation for cardiovascular applications; among the most popular techniques we can mention the Kalman filtering approaches or the variational procedures.[5,15,38] For our specific analysis, it is essential to account for the correct boundary data on the solid wall geometries. This problem has been already addressed by Crosetto *et al.*[14] and Moireau *et al.*[39] for the external surface of the arterial wall, where Robin boundary conditions have been successfully used to account for the elastic and viscoelastic responses of the external tissues. Nevertheless, the values of the empiric tissue parameters appearing at the boundaries is rather difficult to estimate, and neither calibration procedures nor sensitivity analysis to show the effect of the variation of the parameters on the main quantities of interest were provided. Regarding the interface boundary rings of the arterial wall, in Formaggia *et al.*[20] and Malossi *et al.*[37] an approach to prescribe the continuity of the vessel area with surrounding models has been proposed. However, its impact on cardiovascular simulations compared to fixed area configurations has never been investigated, apart from few benchmark tests in simple geometries.

With the aim of covering the aspects mentioned above, in this work we also provide several comparisons and sensitivity analysis focused both on the calibration of the tissue parameters and on the analysis of the impact of different interface ring boundary conditions on the main quantities of interest.

This work is organized as follows. In the "Geometrical Multiscale Approach" section we describe the main ingredients of the geometrical multiscale methodology. Then, in the "Numerical Simulations" section, we present the numerical results with several comparisons and sensitivity analyses. Finally, main conclusions are summarized in the "Conclusions" section.

## GEOMETRICAL MULTISCALE APPROACH

In this section we describe the main components of the geometrical multiscale method that we use to simulate the global arterial circulation. More precisely, we model the arterial network by coupling together different dimensionally-heterogeneous models, such as 3-D FSI models, which are used to represent specific components of main interest, 1-D FSI models, to simulate the pulse wave propagation in the global arterial system, and three-element RCR windkessel terminals, that account for the peripheral circulation and correspond to well known simple differential algebraic equations, for brevity not described here (see Malossi *et al.*[35], Section 5.1 for all the details). Finally, we briefly recall from other works the coupling equations and the numerical approach to solve the global network of models.

### *3-D FSI Model for Main Arteries*

In a geometrical multiscale setting, 3-D FSI models are used to simulate the hemodynamics in complex geometrical situations, such as those occurring at bifurcations, aneurysms, and stenoses among others. In

addition, when aiming at patient-specific analyses, the correct characterization of the local arterial flow has to be carried out by using patient-specific data obtained from medical images, e.g., computed tomography (CT) scan or magnetic resonance imaging (MRI).

*Equations*

Let $\Omega \subset \mathbb{R}^3$ with boundary $\partial\Omega$, where $\bar{\Omega} = \bar{\Omega}_F \cup \bar{\Omega}_S$, being $\Omega_F$ and $\Omega_S$ the fluid and solid domains, respectively. In addition, let $\Gamma_I$ be the fluid-solid interface $\partial\Omega_F \cap \partial\Omega_S$. The FSI problem employed in this work consists of the incompressible Navier–Stokes equations coupled with a linear elastic isotropic structure described by the St. Venant–Kirchhoff equations. To account for the interaction between the fluid and the solid, we define an Arbitrary Lagrangian–Eulerian (ALE) map, i.e.,

$$\mathcal{M}^t : \Omega_F^0 \to \Omega_F^t \subset \mathbb{R}^3$$
$$\mathbf{x}^0 \mapsto \mathcal{M}^t(\mathbf{x}^0) = \mathbf{x}^0 + \mathbf{d}_F(\mathbf{x}^0),$$

where the superscripts 0 and $t$ refer to the reference and current configurations, respectively (see Fig. 1), $\mathbf{x}^0 \in \Omega_F^0$ is a point, and $\mathbf{d}_F$ is the fluid domain displacement. More precisely, in this work we compute $\mathbf{d}_F$ as the harmonic extension of the solid displacement $\mathbf{d}_S$ at the reference fluid-solid interface $\Gamma_I^0$ to the interior of the reference fluid domain $\Omega_F^0$.

The resulting FSI problem reads

$$\begin{cases} \left.\dfrac{\partial \mathbf{u}_F}{\partial t}\right|_{\mathbf{x}^0} + \left(\left(\mathbf{u}_F - \left.\dfrac{\partial \mathbf{d}_F}{\partial t}\right|_{\mathbf{x}^0}\right)\cdot\nabla\right)\mathbf{u}_F & \\ -\dfrac{1}{\rho_F}\nabla\cdot\sigma_F = \mathbf{0} & \text{in } \Omega_F^t \times (0,T], \\ \nabla\cdot\mathbf{u}_F = 0 & \text{in } \Omega_F^t \times (0,T], \\ \rho_S \dfrac{\partial^2 \mathbf{d}_S}{\partial t^2} - \nabla\cdot\sigma_S = \mathbf{0} & \text{in } \Omega_S^0 \times (0,T], \\ -\Delta \mathbf{d}_F = \mathbf{0} & \text{in } \Omega_F^0 \times (0,T], \\ \mathbf{u}_F \circ \mathcal{M}^t - \dfrac{\partial \mathbf{d}_S}{\partial t} = \mathbf{0} & \text{on } \Gamma_I^0 \times (0,T], \\ \sigma_S \cdot \mathbf{n}_S - J_S G_S^{-T}(\sigma_F \circ \mathcal{M}^t)\cdot \mathbf{n}_S = \mathbf{0} & \text{on } \Gamma^0 \times (0,T], \\ \mathbf{d}_F - \mathbf{d}_S = \mathbf{0} & \text{on } \Gamma_I^0 \times (0,T], \end{cases} \tag{1}$$

where $(0,T)$ is the time interval, $\mathbf{u}_F$ the fluid velocity, $\rho_F$ and $\rho_S$ are the fluid and solid density, respectively, $\mathbf{n}_S$ is the outgoing normal direction applied to the solid domain, $G_S = I + \nabla \mathbf{d}_S$ the solid deformation gradient (with I the identity matrix), and $J_S = \det(G_S)$. In addition, $\sigma_F$ and $\sigma_S$ are the Cauchy and the first Piola–Kirchhoff stress tensors, respectively, i.e.,

$$\sigma_F = -p_F I + 2\mu\epsilon_F(\mathbf{u}_F),$$
$$\sigma_S = \lambda_S(E_S, \nu_S)\mathrm{tr}(\epsilon_S(\mathbf{d}_S))I + 2\mu_S(E_S, \nu_S)\epsilon_S(\mathbf{d}_S),$$

where $\epsilon_F(\mathbf{u}_F)$ is the strain rate tensor, being $p_F$ the fluid pressure and $\mu_F$ the fluid dynamic viscosity, and $\epsilon_S(\mathbf{d}_S)$ is the linear strain tensor, being $\lambda_S$ and $\mu_S$ the first and second Lamé parameters, respectively, which are algebraic functions of the Young's modulus $E_S$ and the Poisson's ratio $\nu_S$ of the wall material.

Problem (1) is closed by a proper set of initial and boundary conditions. More precisely, on the external wall $\Gamma_{S,ext}^0$ we apply a viscoelastic Robin boundary condition to account for the presence of the external tissues, as we detail in the "Robin Boundary Condition for the Solid External Wall" section. On $\Gamma_{F,j}^t \subset \partial\Omega_F^t \backslash \Gamma_I^t$, $j = 1, \ldots, n_{FS}^\Gamma$ we impose either inflow and outflow boundary data or continuity equations with the surrounding models, which are detailed in the "Interface Equations for the Global Network of Models" section. Similarly, the inlet/outlet solid rings $\Gamma_{S,j}^0$, $j = 1, \ldots, n_{FS}^\Gamma$ can be either fixed or scaled to match the area of surrounding models, as described by Malossi *et al.*[37] and briefly recalled in the "Interface Equations for the Global Network of Models" section.

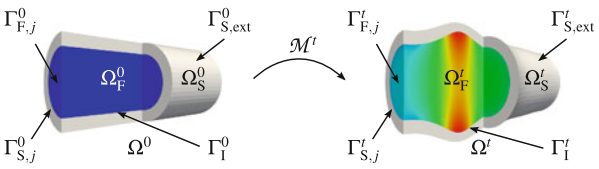


**FIGURE 1. ALE map between reference and current configurations. The colors in the scheme refer to the computed pressure field.**

**Remark 1** Several models of the arterial wall are described in literature, with different levels of complexity.[24,27,28,32,44] An accurate model for the arterial wall should take into account the effects of anisotropy due to the distribution of the collagen fibers, the three layers (intima, media, and adventitia) structure, the nonlinear behavior due to collagen activation, and the incompressibility constraint. Nevertheless, a linear elastic isotropic structure is still considered a reasonable approximation for the large healthy arteries, as demonstrated numerically in, e.g., Crosetto *et al.*,[12,14] and validated experimentally in, e.g., Kanyanta *et al.*[29]

*Numerical Approximation*

The FSI problem is solved by using a non-modular (monolithic) approach.[11,13] The fluid problem is discretized in space by a $\mathbb{P}1 - \mathbb{P}1$ finite element method, stabilized by an interior penalty technique.[9] The solid and the geometric problems are discretized in space by $\mathbb{P}1$ finite elements. Regarding time discretizations for the incompressible Navier–Stokes equations on moving domains we use a first order Euler scheme, while for the structural problem we use a second order midpoint scheme, for an overall accuracy of one. The time

interval $[0, T]$ is split into subintervals $[t^n, t^{n+1}]$, $n = 0, 1, 2, \ldots$, such that $t^n = n\Delta t$, $\Delta t$ being the time step. The fluid and solid problems are coupled by using the geometric convective explicit time discretization, i.e., the fluid problem is linearized by considering explicit the fluid domain displacement and the convective term. This choice allows to split the solution of the geometric part (the harmonic extension) from the fluid-solid one, leading to a significant reduction of the computational cost. For more details on the 3-D FSI problem see Crosetto.[11]

*Robin Boundary Condition for the Solid External Wall*

From the modeling point of view, one critical aspect to get physiological results in a 3-D FSI simulation is the tuning of the boundary condition on the solid external wall. The influence of external tissues and organs tethering and constraining the movement of blood vessels is of critical importance when simulating 3-D FSI problems in the arterial system.[33] At the present time, the modeling of the detailed multi-contact relations between the arteries and the other tissues is unfeasible. However, in the literature there are examples proving that the behavior of external tissues support on the outer arterial wall can be handled by enforcing a Robin boundary condition on $\Gamma^0_{S,ext}$. As an example we mention the work of Crosetto *et al.*,[14] where the tissues are modeled with a purely elastic term, and the work of Moireau *et al.*,[39] where both the elastic and the viscoelastic contributions are accounted. In this latter case, the resulting Robin boundary condition for the 3-D FSI problem reads

$$\sigma_S \cdot \mathbf{n}_S + k_S \mathbf{d}_S + c_S \mathbf{v}_S + P_{ext}\mathbf{n}_S = \mathbf{0}, \quad \text{on } \Gamma^0_{S,ext} \times (0, T], \tag{2}$$

where $\mathbf{v}_S$ is the velocity of the solid domain and $P_{ext}$ the reference external pressure. The parameters $k_S$ and $c_S$ account for the elastic and viscoelastic response of the external tissues, respectively. More generally, they are empiric coefficients that depend on space and, possibly, on time (e.g., to represent the change of mechanical properties over time).

Tuning the value of the parameters $k_S$ and $c_S$ is rather difficult. In both Crosetto *et al.*[14] and Moireau *et al.*[39] a range of orders of magnitude for the aorta is identified on the basis of qualitative considerations about the pulse wave velocity and the maximum admissible displacement of the vessel wall. However, neither further investigations nor sensitivity analyses that show the effect of the variation of the parameters on the main quantities of interest are provided. To fill this gap, in the "External Tissues Parameters Comparisons: 3-D Aorta" and "External Tissues Parameters Comparisons: 3-D Iliac" sections we perform several comparisons in terms of flow rate and displacement for the aorta and iliac arteries, respectively, as a function of different sets of values for the parameters $k_S$ and $c_S$.

**Remark 2** From the numerical viewpoint, the Robin boundary condition must be implemented according to the time discretization scheme used in the solid problem. In particular, since in this work we use an explicit second order mid-point scheme, the following relation holds

$$\frac{\mathbf{v}_S^{n+1} + \mathbf{v}_S^n}{2} = \frac{\mathbf{d}_S^{n+1} - \mathbf{d}_S^n}{\Delta t},$$

such that, for $n = 0, 1, 2, \ldots$, the discrete form of (2) reads

$$\sigma_S \cdot \mathbf{n}_S + \left(k_S + \frac{2c_S}{\Delta t}\right)\mathbf{d}_S^{n+1} - \left(\frac{2c_S}{\Delta t}\mathbf{d}_S^n + c_S \mathbf{v}_S^n\right) + P_{ext}\mathbf{n}_S = \mathbf{0}, \quad \text{on } \Gamma^0_{S,ext}.$$

*1-D FSI Model for the Global Arterial Circulation*

In a geometrical multiscale setting, the global arterial circulation can be modeled by a network of 1-D FSI models based on the Euler equations.[16] Despite its simple axial symmetric representation of the blood flow, it has proven to be able to provide accurate information under physiological and pathophysiological conditions, and therefore gives insight about the main characteristics that lead to the interplay among physical phenomena taking place in the systemic arteries.

*Equations*

The 1-D FSI model is derived from the incompressible Navier–Stokes equations by introducing some simplifying hypotheses on the behavior of the flow quantities over the cross-section of the artery. The structural model is accounted through a simple pressure-area relation. Being $z \in [0, L]$ the axial coordinate, with $L$ the length of the vessel, the resulting governing equations are

$$\begin{cases} \dfrac{\partial A}{\partial t} + \dfrac{\partial Q}{\partial z} = 0 & \text{in } (0, \mathrm{L}) \times (0, \mathrm{T}], \\ \dfrac{\partial Q}{\partial t} + \dfrac{\partial}{\partial z}\left(\alpha_F \dfrac{Q^2}{A}\right) + \dfrac{A}{\rho_F}\dfrac{\partial P}{\partial z} & \\ \quad + \kappa_F \dfrac{Q}{A} = 0 & \text{in } (0, L) \times (0, T], \\ P - \psi(A) = 0 & \text{in } (0, L) \times (0, T], \end{cases} \tag{3}$$

where $\alpha_F$ and $\kappa_F$ are the Coriolis and friction coefficients, respectively,[35] $A$ is the cross-sectional area, $Q$ the volumetric flow rate, $P$ the average pressure, and

$$\psi(A) = P_{\text{ext}} + \beta_{\text{S}}\left(\sqrt{\frac{A}{A^0}} - 1\right) + \gamma_{\text{S}}\left(\frac{1}{A\sqrt{A}}\frac{\partial A}{\partial t}\right), \quad (4)$$

where

$$\beta_{\text{S}} = \sqrt{\frac{\pi}{A_0}}\frac{h_{\text{S}}E_{\text{S}}}{1-\nu_{\text{S}}^2}, \quad \gamma_{\text{S}} = \frac{T_{\text{S}}\tan\phi_{\text{S}}}{4\sqrt{\pi}}\frac{h_{\text{S}}E_{\text{S}}}{1-\nu_{\text{S}}^2},$$

being $A^0$ the reference value for the vessel area, $h_{\text{S}}$ the wall thickness, $T_{\text{S}}$ the wave characteristic time, and $\phi_{\text{S}}$ the viscoelastic angle. The second and third terms in (4) account for the elastic and viscoelastic response of the vessel wall.

Problem (3) is finally closed by a proper set of initial and boundary conditions. The latter can be either inflow and outflow boundary data or continuity equations with the surrounding models, as we detail in the "Interface Equations for the Global Network of Models" section.

### *Numerical Approximation*

The 1-D FSI problem is solved by using an operator splitting technique based on an explicit second order Taylor–Galerkin discretization, where the solution of the problem is split into two steps, such that the first one corresponds to the solution of a purely elastic problem, while the second one provides a viscoelastic correction.[19] The spatial discretization is accomplished using $\mathbb{P}1$ finite elements. For more details see Malossi *et al.*[35] and references therein.

### *Interface Equations for the Global Network of Models*

The solution of the global dimensionally-heterogeneous problem is addressed following the approach first devised in Malossi *et al.*[36] and later extended in Malossi *et al.*[37] to account for the continuity of the vessel area. More precisely, let us consider a general network of heterogeneous models connected by $\mathcal{C}$ coupling nodes. At each node we write the conservation of averaged/integrated quantities over the boundary interfaces, such that the interface problem does not have any dependency on the geometrical nature nor on the mathematical formulation of each model. In other words, we treat the coupled models as black boxes, such that the equations and the modeling assumptions (e.g., 3-D vs. 1-D modeling) are hidden behind general interfaces providing information regarding the boundary values in terms of averaged/integrated quantities. Particularly, these boundary quantities are the volumetric flow rate $\mathcal{Q}$, the averaged normal component of the traction vector $\mathcal{S}$, and the area of the fluid section $\mathcal{A}$, hereafter referred to as *coupling flow*, *coupling stress*, and *coupling area*, respectively. On the $j$th coupling interface of the 3-D FSI model these quantities are computed as

$$\mathcal{Q}_j^{\text{3-D}} = \int_{\Gamma^t_{\text{F},j}} \mathbf{u}_{\text{F}}\cdot\mathbf{n}_{\text{F}}\,\mathrm{d}\Gamma, \quad j = 1,\dots,n^{\Gamma}_{\text{FS}},$$

$$\mathcal{S}_j^{\text{3-D}} = \frac{1}{\left|\Gamma^t_{\text{F},j}\right|}\int_{\Gamma^t_{e,j}} (\sigma_{\text{F}}\cdot\mathbf{n}_{\text{F}})\cdot\mathbf{n}_{\text{F}}\,\mathrm{d}\Gamma, \quad j = 1,\dots,n^{\Gamma}_{\text{FS}},$$

$$\mathcal{A}_j^{\text{3-D}} = \left|\Gamma^t_{,j}\right|, \quad j = 1,\dots,n^{\Gamma}_{\text{FS}},$$

where $\mathbf{n}_{\text{F}}$ is the outgoing normal direction applied to the fluid domain. The 3-D FSI fluid problem is closed by imposing $(\sigma_{\text{F}}\cdot\mathbf{n}_{\text{F}})\cdot\boldsymbol{\tau}_{2\text{F}} = 0$ and $(\sigma_{\text{F}}\cdot\mathbf{n}_{\text{F}})\cdot\boldsymbol{\tau}_{2\text{F}} = 0$ on $\Gamma^t_{\text{F},j}, j = 1,\dots,n^{\Gamma}_{\text{FS}}$, where $\boldsymbol{\tau}_{1\text{F}}$ and $\boldsymbol{\tau}_{2\text{F}}$ are the two tangential directions. In addition, we assume that the normal stress $(\sigma_{\text{F}}\cdot\mathbf{n}_{\text{F}})\cdot\mathbf{n}_{\text{F}}$ is constant over the coupling interfaces. Regarding the solid problem, following the approach of Formaggia *et al.*,[20] the vessel area is imposed by prescribing a radial displacement of the internal contour of the $j$th 3-D solid ring, i.e.,

$$\begin{cases} \mathbf{d}_{\text{S}}\cdot\mathbf{n}_{\text{S}} = 0 & \text{on } \Gamma^0_{\text{I}}\cap\Gamma^0_{\text{S},j}\times(0,T], \\ \left[\mathbf{d}_{\text{S}} - \Psi^t_j\left(\mathbf{x}^0 - \mathbf{x}^0_{G,j}\right)\right]\cdot\boldsymbol{\tau}_{1\text{S}} = 0 & \text{on } \Gamma^0_{\text{I}}\cap\Gamma^0_{\text{S},j}\times(0,T], \\ \left[\mathbf{d}_{\text{S}} - \Psi^t_j\left(\mathbf{x}^0 - \mathbf{x}^0_{G,j}\right)\right]\cdot\boldsymbol{\tau}_{2\text{S}} = 0 & \text{on } \Gamma^0_{\text{I}}\cap\Gamma^0_{\text{S},j}\times(0,T], \end{cases}$$

for $j = 1,\dots,n^{\Gamma}_{\text{FS}}$, where $\boldsymbol{\tau}_{1\text{S}}$ and $\boldsymbol{\tau}_{2\text{S}}$ are the two tangential directions lying on $\Gamma^0_{\text{S},j}, j = 1,\dots,n^{\Gamma}_{\text{FS}}$. This corresponds to scale the boundary area preserving its original shape, where the radial scale factor is defined as

$$\Psi^t_j = \sqrt{\frac{\mathcal{A}_j^{\text{3-D}}}{A^0_j}} - 1,$$

being $A^0_j$ and $\mathbf{x}^0_{\text{G},j}$ the reference area of the $j$th coupling interface of the 3-D fluid problem and its geometric center, respectively. Other more general approaches might be employed to weakly prescribe the value of the area on the solid boundary interface. Nevertheless, since in cardiovascular applications the displacement of the vessel is relatively small, thus not far from the original shape, the technique presented here can be considered enough accurate for our analysis. Note that to close the 3-D FSI solid problem, we need to impose an additional boundary condition on $\Gamma^0_{\text{S},j}\backslash\Gamma^0_{\text{I}}\cap\Gamma^0_{\text{S},j}, j = 1,\dots,n^{\Gamma}_{\text{FS}}$, which in our case is $\sigma_{\text{S}}\cdot\mathbf{n}_{\text{S}} = \mathbf{0}$. Regarding the two coupling interfaces of the 1-D FSI model we have

$$\begin{array}{lll} \mathcal{Q}_{\text{L}}^{\text{1-D}} = -Q_{\text{L}}, & \mathcal{S}^{\text{1-D}} = -P_{\text{L}}, & \mathcal{A}^{\text{1-D}} = A_{\text{L}}, \\ \mathcal{Q}_{\text{R}}^{\text{1-D}} = Q_{\text{R}}, & \mathcal{S}_{\text{R}}^{\text{1-D}} = -P_{\text{R}}, & \mathcal{A}_{\text{R}}^{\text{1-D}} = A_{\text{R}}, \end{array}$$

where the subscripts L and R stand for left and right quantities, respectively.

The resulting set of conservation equations for the fluid part of the interface problem is

$$\begin{cases} \sum_{i=1}^{\mathcal{I}_c} \mathcal{Q}_{c,i} = 0, \\ \mathcal{S}_{c,1} - \mathcal{S}_{c,i} = 0, \quad i = 2, \ldots, \mathcal{I}_c, \end{cases} \tag{5}$$

where $\mathcal{I}_c$ is the number of interfaces connected by the $c$th coupling node, $c = 1, \ldots, \mathcal{C}$. More precisely, the first equation ensures the conservation of the mass and the second implies the continuity of the mean normal stress. Note that no assumption is made on the type of boundary data ($\mathcal{Q}$ or $\mathcal{S}$) to be imposed on the 3-D and 1-D interfaces. Indeed, our methodology allows to choose the type of data to be applied on any boundary interface independently of the models type.[36,37] The iterations number of the interface problem might be slightly affected by the type of boundary data imposed on the interface of the coupled models. Particularly, in all the tested cases, at a given time step the increase/decrease of the iterations number is always bounded to one or two iterations maximum, without a precise correlation with the chosen type of boundary data. By averaging the number of iterations per time step over the entire simulation, this difference further reduces and becomes nearly negligible.

**Remark 3** Being written in terms of mean normal stress, the set of interface equations (5) does not preserve the total energy of the problem at the interface between two dimensionally-heterogeneous models. However, the kinetic contribution of the total stress is negligible for cardiovascular problems, as shown by Malossi,[34] see Section 5.4.2.5 of the dissertation, such that the results presented here using (5) coincides with those that would have be obtained by prescribing the continuity of the mean total normal stress. Hence, the set of interface equations used in this work are stable for this class of problems.

In case the continuity of the vessel area is enforced between two vessels, the set of Eqs. (5) becomes

$$\begin{cases} \mathcal{Q}_{c,1}^{\text{1-D}} + \mathcal{Q}_{c,2}^{\text{3-D}} = 0, \\ \mathcal{S}_{c,1}^{\text{1-D}} - \mathcal{S}_{c,2}^{\text{3-D}} = 0, \\ \mathcal{A}_{c,1}^{\text{1-D}} - \mathcal{A}_{c,2}^{\text{3-D}} = 0, \end{cases} \tag{6}$$

where, for the sake of clarity, the model to which each quantity belongs is indicated in the superscript. More precisely, the continuity of the vessel area cannot be imposed between two 1-D FSI vessels. In fact, due to modeling reasons, the 1-D FSI problem needs just one physical boundary condition on each side of the segment, and therefore it is not possible to impose both a fluid quantity and the vessel area at the same time. On the contrary, the 3-D FSI model needs boundary data on both the fluid and the solid parts of each interface, such that it is possible to set the continuity of its boundary areas with the surrounding 1-D FSI models. In addition, we remark that (6) is written for the specific case of a 3-D FSI interface coupled with a single 1-D FSI model. In the case of a generalization to two or more 1-D models connected to the same 3-D FSI interface, the continuity of the area does not make sense, and for this reason we do not address this case.[37]

From the numerical viewpoint, the global interface problem is written in a residual formulation and solved by using the Newton and the Broyden methods. First of all, the Jacobian of the global interface problem is either computed analytically by solving the tangent problem associated to each model, or approximated with finite differences. The resulting matrix is used to perform a single (inexact-)Newton iteration, which corresponds to the very first iteration at the first time step of the simulation. After that, from the second iteration and for all the other time steps, the Jacobian is updated by using a Broyden method, which is based on a cheap evaluation of the residual of the interface problem.[34,35,37]

## NUMERICAL SIMULATIONS

In this section we present several comparisons among different geometrical multiscale models. The purpose of these comparisons is manifold. On the one hand, we study the interaction between 3-D patient specific geometries and a global arterial network of 1-D models. This results are compared both with a full 1-D network of arteries, and a stand-alone 3-D simulation with boundary data taken from the same full 1-D network. On the other hand, we also analyze the effect of the 3-D solid boundary conditions on the simulations. In particular, we perform a sensitivity analysis of the external tissues parameters, and we also compare results of configurations where the area at the interfaces is fixed, with those where it is scaled to have the continuity of the vessels size with the surrounding 1-D arteries.

All the simulations presented in this work have been performed using the LifeV library[1] on several cluster nodes with two Intel® Xeon® processors X5550 (quad core, 8 MB cache, 2.66 GHz CPU) each, interconnected by a 20 Gb/s InfiniBand® architecture.

### *Human Arterial Tree Model*

To model the global circulation we use the data of the arterial network provided in Reymond *et al.*,[43] which is composed by 103 elements (4 coronary, 24 aortic, 51 cerebral, 10 upper limbs, and 14 lower limbs) and includes all the values of the parameters required to describe the blood flow, such as the geometrical properties of the vessels (length and proximal/distal areas)

[1] http://www.lifev.org.

**TABLE 1. Main parameters of the 1-D network of arteries.**

| | | |
|---|---|---|
| $\rho_F$ | Blood density | 1.04 g/cm$^3$ |
| $\mu_F$ | Blood viscosity | 0.035 g/cm/s |
| $\kappa_F$ | Friction coefficient | 2.326 cm$^2$/s |
| $\alpha_F$ | Coriolis coefficient | 1.1 |
| $P_{ext}$ | Reference external pressure | 100,000 dyn/cm$^2$ |
| $P_v$ | Venous pressure | 6,666 dyn/cm$^2$ |
| $h_S/R_S$ | Wall thickness/local radius | 0.1 |
| $E_S$ | Young's modulus | 3–12 $\times$ 10$^6$ dyn/cm$^2$ |
| $\nu_S$ | Poisson's ratio | 0.50 |
| $\phi_S$ | Viscoelastic angle | 10° |
| $T_S$ | Systolic period | 0.24 s |
| | Heart rate | 75 bpm |

For more details see Malossi *et al.*[35] and references therein.

and the data for the terminals, which are modeled as three-element windkessel elements and account for the cumulative effects of all distal vessels (small arteries, arterioles, and capillaries). These values have been obtained both from *in vivo* measurements and averaged data from the literature. The presence of the venous circulation is taken into account by imposing the return venous pressure $P_v$ on the distal side of each windkessel terminal node. Regarding the parameters of the wall, since we use a different model, we estimate these values from other sources.[35] The main parameters that define the problem are summarized in Table 1. The average space discretization of each 1-D FSI segment is 0.1 cm. Regarding the time discretization, in each artery we define a different time step based on the local CFL requirements. These local inner time steps are defined such that they synchronize with each other at each global outer time step, i.e., the time step chosen for the 3-D FSI models. This guarantee the possibility to write the interface equations between all the coupled models at each outer time step. More details about this two-level adaptive time step technique are provided in Malossi *et al.*[35]

### *Geometry Reconstruction and Mesh Generation*

In this work we use the 3-D FSI model to simulate the flow in two main patient-specific arteries, i.e., the aorta and the iliac of two healthy patients. These geometries have several bifurcations and some severe bends, such that the blood flow dynamics can be precisely described only by employing a 3-D model.

The segmentation of the aorta was obtained through MRI Time of Flight acquisition on a 3T MRI scanner (Siemens Trio-Tim 3T System); details on the used sequences are given in Reymond *et al.*[42] Then, the arterial lumen was reconstructed in 3-D from MRI magnitude data (ITK Snap software). Since the thickness of the wall is not visible in MRI data, it had to be synthetically reconstructed. In particular, it has been estimated to be equal to 10 percent of local lumen radius, which is a commonly accepted approximation.[31] Regarding the iliac, the geometry of the lumen has been taken from the Simtk website,[2] and the thickness of the wall has been reconstructed with the same assumptions used for the aorta.

To correctly model the different material properties of the arterial wall and of the external tissues, we divide the solid domains into several regions, which are schematically shown in Fig. 2. Note that for the iliac geometry we provide two different configurations, which are later used in the "External Tissues Parameters Comparisons: 3-D Iliac" section for a numerical comparison of the results as a function of the tissue parameters at the bifurcations. The main wall parameters that define the 3-D problems are summarized in Table 2.

**Remark 4** The jumps in the mechanical properties of the arterial wall (see Fig. 2 and Table 2) might introduce wave reflections in the flow field. Nevertheless, these reflections are negligible if compared to the physical reflection driven by the sudden change in the vessel lumen at the bifurcations. Moreover, the structural model can be easily refined by introducing smooth continuous functions between the different wall regions. This improvement will be included in future works.

**Remark 5** The value of the arterial wall density has been taken from Crosetto *et al.*[13] and Moireau *et al.*[39] In Malossi,[34] see Section 5.4.2.6 of the dissertation, a comparison of the results obtained by setting $\rho_S = 1.2$ g/cm$^3$, with those computed by using either $\rho_S = 1.0$ g/cm$^3$[46,47] or $\rho_S = 0.0$ g/cm$^3$ (purely elastic wall without inertia) is presented, proving that (i) the inertia of the arterial wall has a very small impact on this class of applications, and (ii) the methodology and algorithms described in Section 2 are stable even if the arterial wall density is neglected.

Finally, for each arterial vessel two separate conforming fluid and solid geometries have been generated using the VTK,[3] VMTK,[4] and ITK[5] libraries.[17] The resulting mesh of the fluid part of the 3-D aorta consists of 280,199 unstructured tetrahedral elements with 50,866 vertices, while the solid part is made of 278,904 structured tetrahedral elements with 58,565 vertices. The corresponding average space discretizations for both the fluid and solid problems is 0.158 cm. Regarding the 3-D iliac, the mesh of the fluid part

[2] http://simtk.org.
[3] http://www.vtk.org.
[4] http://www.vmtk.org.
[5] http://www.itk.org.

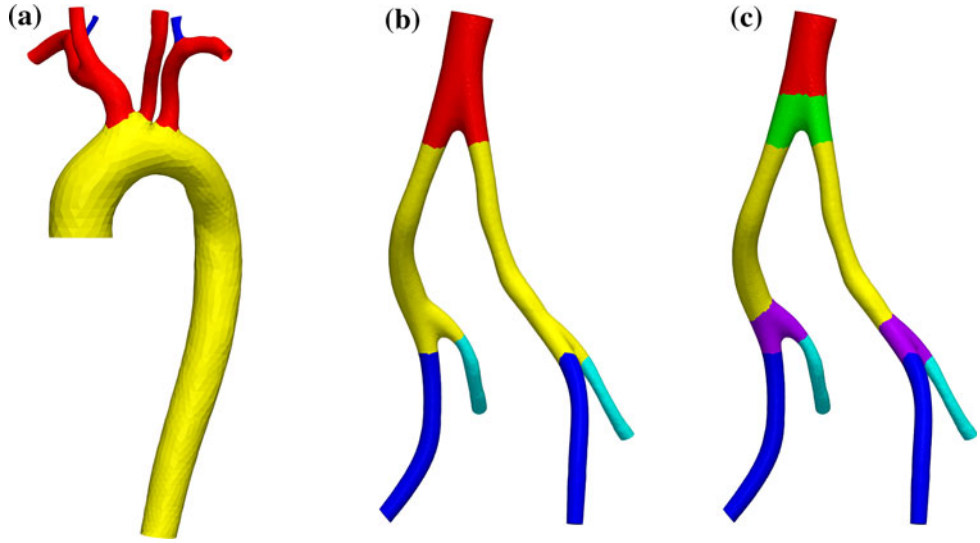


**FIGURE 2. View of the aorta and iliac geometries with wall regions. (a) The aorta is divided in three regions: aortic arch (yellow), carotids and subclavians (red), and vertebrals (blue). (b) The iliac is divided in four regions: abdominal aorta (red), common iliac (yellow), external iliac (blue), and inner iliac (cyan). (c) Same as (b) with two additional regions at the bifurcations: abdominal aorta bifurcation (green) and common iliac bifurcations (magenta).**

**TABLE 2. Wall parameters of the 3-D FSI arteries.**

| | | |
|---|---|---|
| $\rho_S$ | Wall density | 1.2 g/cm$^3$ |
| $h_S/R_S$ | Wall thickness/local radius | 0.1 |
| $E_S$ | Young's modulus | 3–12 $\times$ 10$^6$ dyn/cm$^2$ |
| $\nu_S$ | Poisson's ratio | 0.48 |

The Young's modulus of the 3-D FSI aorta and iliac is 3,000,000 dyn/cm$^2$ in all the branches apart from the vertebral arteries, where it is 6,000,000 dyn/cm$^2$, and inner iliac arteries, where it is 12,000,000 dyn/cm$^2$.

consists of 350,376 unstructured tetrahedral elements with 63,716 vertices, while the solid part is made of 359,256 structured tetrahedral elements with 60,788 vertices. In this case, the corresponding average space discretizations for both the fluid and solid problems is 0.076 cm. Regarding the time discretization, we use a constant time step of 0.001 s.

**Remark 6** The mesh size employed for the discretization of the 3-D geometries used in our studies might not be fine enough to represent the smallest fluid dynamics structures. Particularly, the relatively high Reynolds number in the aorta requires the use of boundary layers to capture the details of the fluid dynamics near the wall (which are fundamental to evaluate, e.g., the wall shear stress). Nevertheless, the focus of our analysis is on the value of the averaged/integrated interface quantities, such as the flow rate, the inlet/outlet pressure drop, and the boundary wall displacement, for which the employed discretization is fine enough.

### *Geometrical Multiscale Modeling*

In this section we set up and solve three different geometrical multiscale models where the 3-D patient-specific vessels in Fig. 2 are embedded in the 1-D network described in the "Human Arterial Tree Model" section, which represents an average healthy patient.

To set up the models we use the following procedure. First of all, we identify the 1-D elements of the network to be removed or cut, since they overlap with some regions of the 3-D patient-specific geometries. This is done by measuring the length of the different branches of the 3-D vessels and comparing these data with the one of the 1-D network. Obviously, this phase presents several degrees of freedom and arbitrariness. The degree of precision of this step also depends on the region of interest and the required level of accuracy (e.g., rough evaluation of flow vs. precise local quantification for surgery planning). In a clinical context this operation should be supervised by the clinician in order to immediately determine the crucial regions for the numerical simulations. Once the 1-D elements are cut, the second step consists in changing the reference area and the wall thickness of the 1-D arteries in order to match the one of the nearby 3-D interfaces. Since the 3-D geometries are not symmetric, it is possible that some asymmetries are introduced also in the 1-D networks (e.g., between the left and right external iliac arteries). Moreover, it is important to check that the resulting distal area is always smaller or equal than the proximal one. If it is not the case, some further adjustments to the 1-D elements are required to avoid a non-physiological behavior of the flow in those elements.

*Parallel Solution of the Global Problem*

The parallelism is handled by distributing the models across the available processes and cluster nodes. Each model can be either assigned to a single process or partitioned across several nodes. In our implementation, we distribute the models as a function of their type and computational cost. More precisely, the models obtained through a dimensional reduction (e.g., 1-D FSI models and the lumped parameters terminals) are distributed one per each available process. If the number of models exceeds the number of processes, the algorithm assigns more models to the same process. For examples, when solving a network of 150 1-D and/or lumped parameters models using 48 processes, each process holds at least 3 models. The more expensive 3-D FSI models are then partitioned across all the available nodes and processes (including those that are already holding one or more reduced dimensional models). If more 3-D models are present in the network, each of them is split on a subset of nodes such that they globally use all the available resources. Thanks to the parallelism intrinsic in our algorithms, this choice leads in general to a balanced load.

The global network of elements is solved by using the Broyden method, as described at the end of the "Interface Equations for the Global Network of Models" section. The convergence to the imposed tolerance of $10^{-6}$ is achieved between 2 and 4 iterations; the average number of iterations per time step is approximately 2.25 in all the presented cases.

*External Tissues Parameters Comparisons: 3-D Aorta*

In this section we focus on the study of the external tissues parameters $k_S$ and $c_S$ introduced by the Robin boundary condition on the arterial wall of the 3-D FSI problem. For this analysis, we consider a geometrical multiscale model assembled by coupling the 3-D patient-specific aorta in Fig. 2a with the 1-D arterial tree described in the "Human Arterial Tree Model" section, which represents an average healthy patient. For the sake of simplicity, the results presented in this section are obtained by fixing the position of the boundary solid rings of the 3-D arterial wall of the aorta, i.e., $\mathbf{d}_S = \mathbf{0}$ on $\Gamma^0_{S,j}, \quad j = 1, \ldots, n^{\Gamma}_{FS}$.

The first study we perform consists of a sensitivity analysis of the main quantities of interest with respect to a variation of the elastic parameter $k_S$. This is done by assuming $c_S = 0$ dyn s/cm$^3$ and choosing five sets of values for the coefficient $k_S$ at the different branches of the aorta, as detailed in Table 3. Note that the values of the different cases are chosen as multiples of those of case $E^A_1$.

The results of this comparison, at the most significant coupling interfaces between the 3-D aorta and the 1-D network, are summarized in Fig. 3, where we also plot the result of the full 1-D arterial network. First of all, we observe that the behavior of the flow rate and pressure is quite different in each of the five considered cases. From the behavior of the pressure we observe that the elastic tissues parameters of case $E^A_1$ is not stiff enough to correctly capture the cardiovascular wave pulse (the pressure level is low and nearly flat). This is confirmed by the analysis of the displacement magnitude field of the 3-D arterial wall of the aorta at the second heart beat (see Fig. 4), where we observe a small overinflation of the thoracic aorta in case $E^A_1$ and severe overinflations of the left common carotid artery for the first three sets of coefficients in Table 3.

The analysis of the flow rate profiles in the other branches displayed in Fig. 3 shows that all the considered cases present spurious high-frequency oscillations at the vertebral arteries, which are probably the cause of the numerical breakdown in cases $E^A_2$ and $E^A_4$. In case $E^A_5$, which represents the stiffest artery, the oscillations do not appear in the left vertebral artery, suggesting that this phenomenon might be related to the stiffness of the external tissues parameters. In particular, the two vertebral arteries are the smallest branches of the considered geometry, which in turn means that the wall thickness there is considerably smaller than in the other branches (we recall that the thickness of the solid domain is chosen to be proportional to the local lumen of the vessel). This could explain the fact that the high-frequency oscillations are not present in the other branches of the same geometry.

**Remark 7** Here, as well as in the forthcoming "External Tissues Parameters Comparisons: 3-D

**TABLE 3. Empirical external tissues coefficients at the different wall regions of the 3-D aorta (see Fig. 2a).**

| | $k_S$ (dyn/cm$^3$) | | | | | |
|---|---|---|---|---|---|---|
| Artery | $E^A_1$ | $E^A_2$ | $E^A_3$ | $E^A_4$ | $E^A_5$ | $c_S$ (dyn s/cm$^3$) |
| Aortic arch | 15,000 | 30,000 | 45,000 | 60,000 | 75,000 | 0.0 |
| Left/right carotid and subclavian | 22,500 | 45,000 | 67,500 | 90,000 | 112,500 | 0.0 |
| Left/right vertebral | 30,000 | 60,000 | 90,000 | 120,000 | 150,000 | 0.0 |

We define five cases for the sets of values of the elastic coefficient.

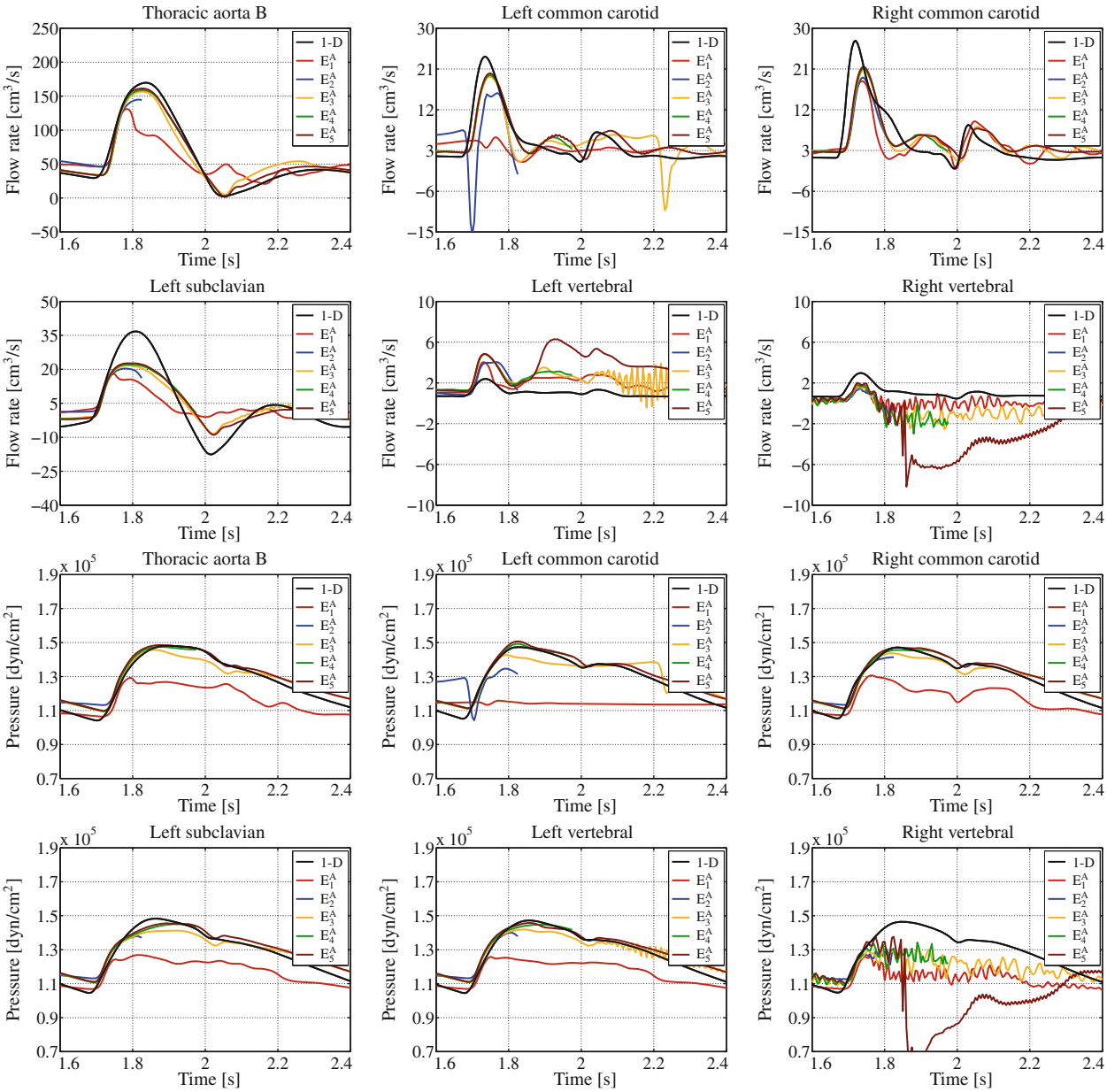


**FIGURE 3. Flow rate and pressure comparison, at the third heart beat, for the sets of values given in Table 3 (elastic behavior of the external tissues), at the most significant coupling interfaces between the 3-D aorta (see Fig. 2a) and the 1-D network. The black line is the solution of the full 1-D network.**

Iliac" section, the results of the full 1-D network are aimed to provide a reference, validated[43] value for the main quantities of interest, and must not be considered as a reference exact solution. Indeed, differences between the results of the geometrical multiscale models and those of the full 1-D network are expected in view of the patient-specific topologies of the 3-D geometries embedded in the former models.

Further comments about the high-frequency oscillations observed in the purely elastic case can be performed by studying the results of a second set of simulations in which we introduce the viscoelastic response of the tissues through the parameter $c_S$ (see Eq. (2)). As previously done for the elastic parameter, we select several sets of values for the coefficient $c_S$ at the different branches of the aorta, as detailed in Table 4. Regarding the elastic parameter, we choose the set of values $E_4^A$, which has proven to be stiff enough to prevent excessive strain in all the branches of the 3-D geometry (see Fig. 4), even if it was not able to smooth out the high-frequency oscillations observed in the smallest branches.

The results of this comparison, at the same interfaces of the previous one, are summarized in Fig. 5.

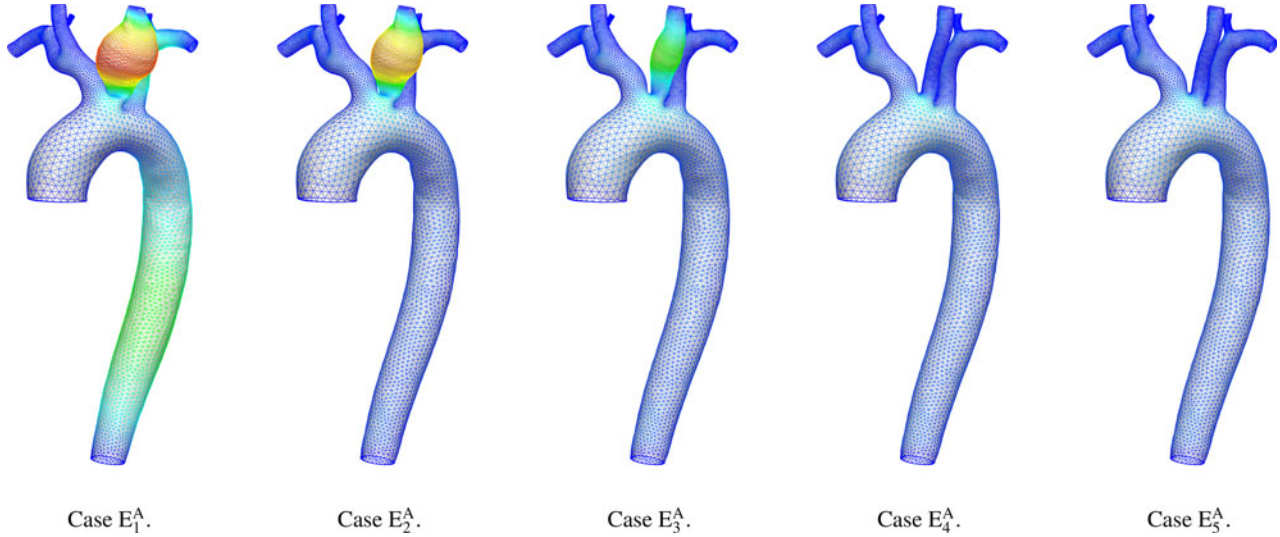


**FIGURE 4. Wall displacement magnitude comparison, at the end-systole of the second heart beat ($t = 1.2$ s), for the sets of values given in Table 3 (elastic behavior of the external tissues) of the 3-D aorta (see Fig. 2a) coupled with the 1-D network (not shown). The color bar ranges from blue (0.0 cm) to red (1.8 cm).**

**TABLE 4. Empirical external tissues coefficients at the different wall regions of the 3-D aorta (see Fig. 2a).**

| | $k_S$ (dyn/cm$^3$) | $c_S$ (dyn s/cm$^3$) | | | | | |
|---|---|---|---|---|---|---|---|
| Artery | $E_4^A$ | $V_1^A$ | $V_2^A$ | $V_3^A$ | $V_4^A$ | $V_5^A$ | $V_6^A$ |
| Aortic arch | 60,000 | 500 | 1,000 | 5,000 | 10,000 | 50,000 | 100,000 |
| Left/right carotid and subclavian | 90,000 | 500 | 1,000 | 5,000 | 10,000 | 50,000 | 100,000 |
| Left/right vertebral | 120,000 | 500 | 1,000 | 5,000 | 10,000 | 50,000 | 100,000 |

We define six cases for the sets of values of the viscoelastic coefficient.

First of all, we observe that the spurious high-frequency oscillations disappear at all the boundary interfaces and independently of the chosen set of values for the parameter $c_S$. This behavior confirms the importance of including the viscoelastic effects in the model of the arterial wall, not only in 1-D FSI simulations, as already proven, for instance, by Malossi *et al.*,[35] but also in 3-D FSI problems, as claimed by Moireau *et al.*[39] Moreover, this result suggests that the high-frequency oscillations observed in Fig. 3 might be related mainly to the model chosen for the structure of the arterial wall. In particular, we recall that in our simulations we use a linear elastic isotropic model, which does not include any damping effect.

Regarding the value of the viscoelastic parameter, we observe that the flow rate and pressure waveforms change significantly among the simulated cases. More precisely, the set of values $V_1^A$ and $V_2^A$, are not high enough to smooth the low-frequency oscillations of the 3-D FSI elastic wall. Moreover, they lead to a pressure overshoot at most of the branches during the systolic peak. On the contrary, the results given by the other four sets of values are all very similar and belong to the physiological regime. In particular, we observe a sort of limit behavior of the viscoelastic parameter, such that above a certain threshold the sensitivity of the flow rate and pressure waveform to a variation of the parameter $c_S$ becomes very small. This is coherent with the nature of the Robin boundary conditions, whose contribution decrease drastically when the parameters value become high. In view of these results, hereafter we compute the value of the viscoelastic parameter as one tenth of the value of the corresponding elastic one, i.e.,

$$c_S = k_S/10. \tag{7}$$

This rule provides a reliable and easy way to calibrate the viscoelastic parameter of the Robin boundary condition for the external tissues.

### *External Tissues Parameters Comparisons: 3-D Iliac*

In this section we further extend the study of the external tissues parameters $k_S$ and $c_S$ by considering a

different problem. More precisely, we set up a geometrical multiscale model composed by the 3-D patient-specific iliac in Fig. 2b coupled with the 1-D arterial tree described in the "Human Arterial Tree Model" section, which represents an average healthy patient. For the sake of simplicity, the results presented in this section are obtained by fixing the position of the boundary solid rings of the 3-D arterial wall of the iliac, i.e., $\mathbf{d}_S = \mathbf{0}$ on $\Gamma^0_{S,j}, j = 1, \ldots, n^{\Gamma}_{FS}$.

First of all, we perform a sensitivity analysis of the main quantities of interest with respect to a variation of the external tissues parameters. In view of the results achieved in the previous section, we directly consider both the elastic and viscoelastic coefficients. For the first one, we choose five sets of values at the different branches of the iliac, as detailed in Table 5. Note that the values of the different cases are chosen as multiples of the ones of case $E^{\mathrm{I}}_1$. Then, following the result of the

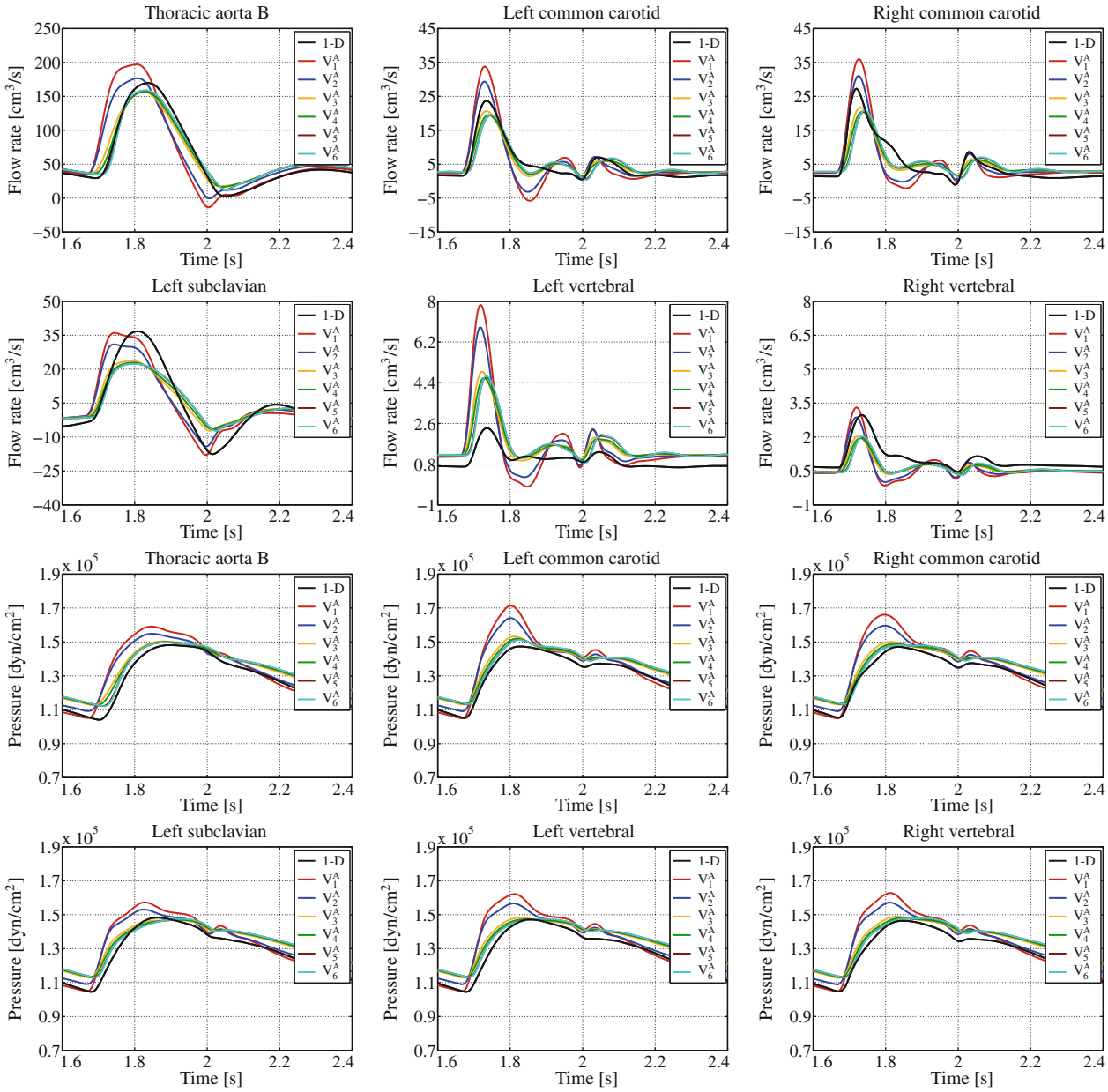


**FIGURE 5. Flow rate and pressure comparison, at the third heart beat, for the sets of values given in Table 4 (elastic and viscoelastic behavior of the external tissues), at the most significant coupling interfaces between the 3-D aorta (see Fig. 2a) and the 1-D network. The black line is the solution of the full 1-D network.**

**TABLE 5. Empirical external tissues coefficients at the different wall regions of the 3-D iliac (see Fig. 2b).**

| | $k_S$ (dyn/cm$^3$) | | | | | |
|---|---|---|---|---|---|---|
| Artery | $E^I_1$ | $E^I_2$ | $E^I_3$ | $E^I_4$ | $E^I_5$ | $c_S$ (dyn s/cm$^3$) |
| Abdominal aorta | 25,000 | 50,000 | 75,000 | 100,000 | 125,000 | $k_S$/10 |
| Left/right common iliac | 35,000 | 70,000 | 105,000 | 140,000 | 112,500 | $k_S$/10 |
| Left/right external iliac | 37,500 | 75,000 | 112,500 | 150,000 | 187,500 | $k_S$/10 |
| Left/right inner iliac | 42,500 | 85,000 | 127,500 | 170,000 | 212,500 | $k_S$/10 |

We define five cases for the sets of values of the coefficients.

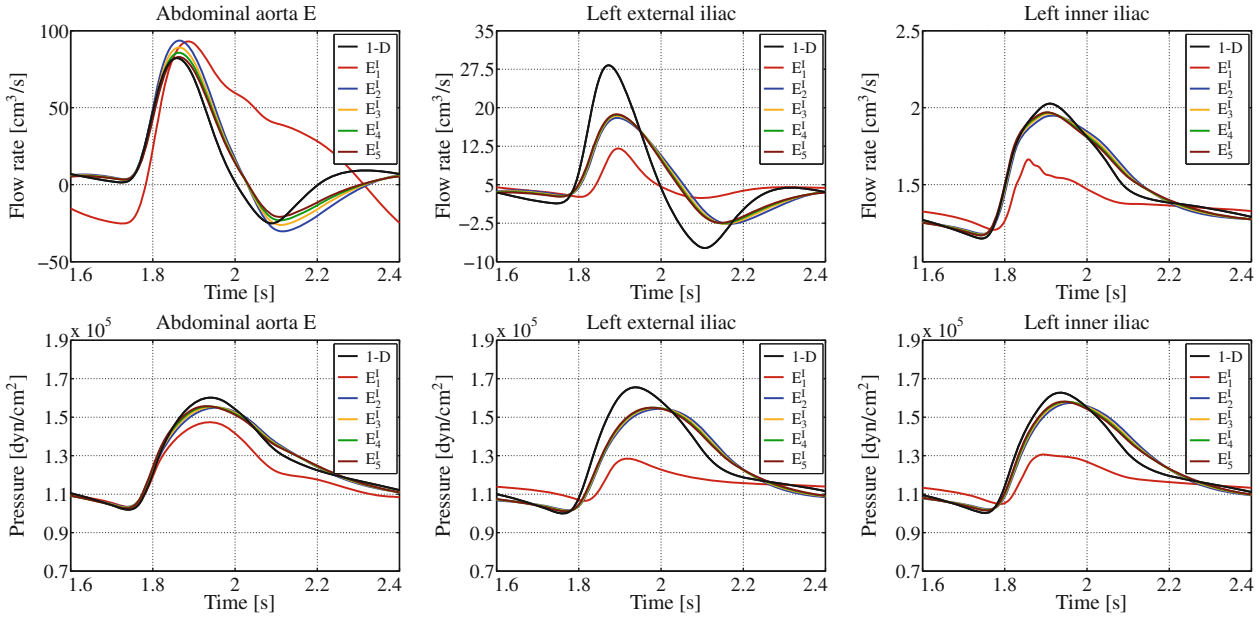


**FIGURE 6. Flow rate and pressure comparison, at the third heart beat, for the sets of values given in Table 5 (elastic and viscoelastic behavior of the external tissues), at the most significant coupling interfaces between the 3-D iliac (see Fig. 2b) and the 1-D network. The black line is the solution of the full 1-D network.**

previous section, the viscoelastic parameter is obtained from (7).

The results of this comparison, at the most significant coupling interfaces between the 3-D iliac and the 1-D network, are summarized in Fig. 6. There we observe that, apart from case $E^I_1$, whose tissues are clearly not stiff enough (the pressure level is significantly lower than the reference one), all the other cases lead to results in a physiological regime. Moreover, there are no significant differences among the last four cases, even if the parameters change considerably. This confirms the results of the previous section. In particular, we remark that the high sensitivity observed in Fig. 3 for the aorta was mainly due to the lack of damping terms and, consequently, to the high-frequency oscillations in the solution, rather than to a true sensitivity to the elastic parameter $k_S$.

Regarding the displacement of the 3-D arterial wall, similarly to the previous section, we observe a gradual decrease in the displacement magnitude with respect to an increase in the value of the tissues parameters. No overinflations appear along the iliac branches in all the simulated cases. However, even in the stiffest case, we observe some severe overinflations at all the three bifurcations. This non-physiological behavior is due to the local reduced stiffness of the vessel, which in turn is caused by the fact that at the branching points the lumen of the vessel increases significantly, while the thickness of the wall gradually diminish (since the distal branches have a smaller radius). In the real patient, these large deformations are prevented thanks to the support of the external tissues and to the presence of collagen fibers, which are not accounted in our model.

To solve this issue without introducing a more complex model for the 3-D vessel wall, we use a second configuration of the iliac geometry, where two additional regions are introduced at the bifurcations (see

**TABLE 6. Empirical external tissues coefficients at the bifurcations of the 3-D iliac (green and magenta wall regions in Fig. 2c).**

| | $k_S$ (dyn/cm$^3$) | | | | |
|---|---|---|---|---|---|
| Artery | $E^I_4$ | $E^I_{4a}$ | $E^I_{4b}$ | $E^I_{4c}$ | $c_S$ (dyn/cm$^3$) |
| Abdominal aorta (bifurcation) | 100,000 | 200,000 | 300,000 | 400,000 | $k_S$/10 |
| Left/right common iliac (bifurcations) | 140,000 | 280,000 | 420,000 | 560,000 | $k_S$/10 |

From the reference case $E^I_4$ (see Table 5), we define three additional configurations.

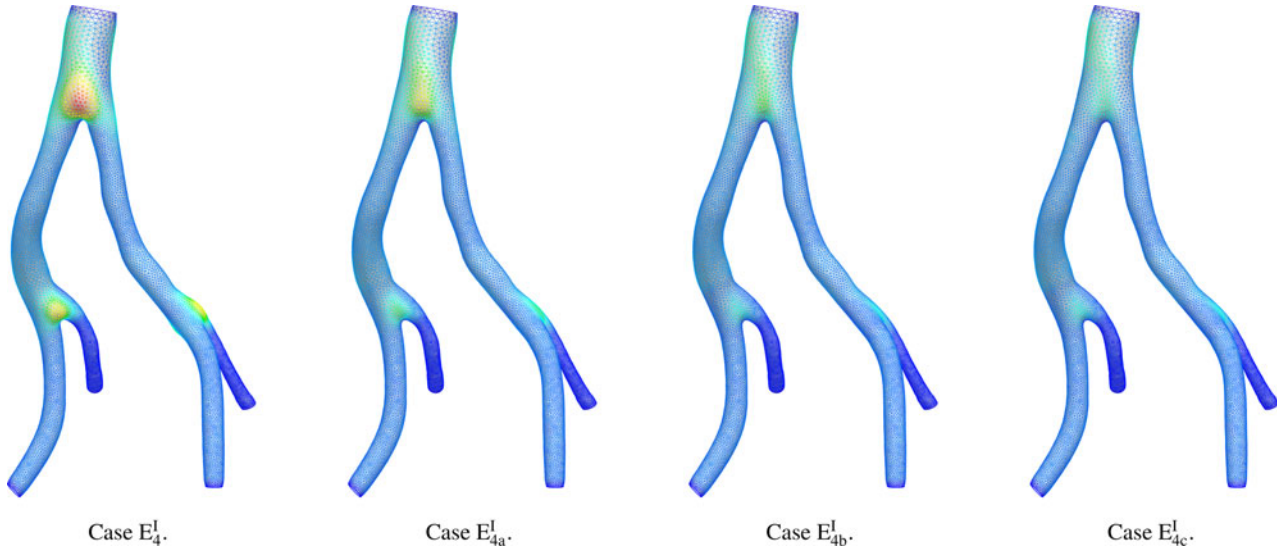


**FIGURE 7. Wall displacement magnitude comparison, at the end-systole of the third heart beat ($t$ = 2.0 s), for the sets of values given in Table 6 (stiffening of the bifurcations), of the 3-D iliac (see Fig. 2c) coupled with the 1-D network (not shown). The color bar ranges from blue (0.0 cm) to red (0.5 cm).**

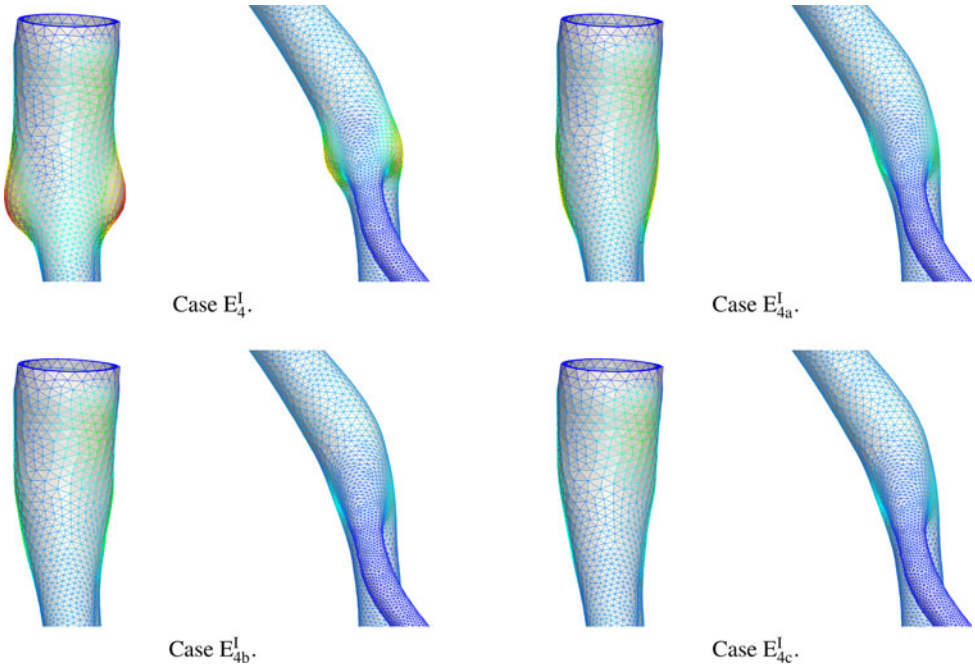


**FIGURE 8. Lateral view of the top and low left bifurcations for the four cases in Fig. 7.**

Fig. 2c). Then we choose case $E_4^{\mathrm{I}}$ as the reference one, and we introduce three additional sets of values for the tissues parameters at the iliac bifurcations, as detailed in Table 6. As before, the values of the different cases are chosen as multiples of the reference one.

In Fig. 7 we compare the magnitude of the displacement field of the 3-D iliac arterial wall for the different cases. The graphs show that at each increase in the values of the tissues parameters, the overinflations at the branches diminish. This phenomenon is more visible in Fig. 8, where an enlarged lateral view of the top and low left bifurcations is shown. In addition, a further analysis of the flow rate and pressure waveform at the coupling interfaces (which for brevity is not presented here) shows no significant changes compared to the results in Fig. 6. In view of these results we conclude that, despite their simple formulation, Robin boundary data provide a reliable way to account for the effect of external tissues over the arterial wall. Moreover, they can be used to somehow compensate a local lack of stiffness due to particular geometrical topologies, at least in healthy arteries.

### *Solid Ring Boundary Condition Comparisons*

In this section we compare the solution of geometrical multiscale models in which the boundary solid rings of the 3-D geometries are fixed, as opposed to the

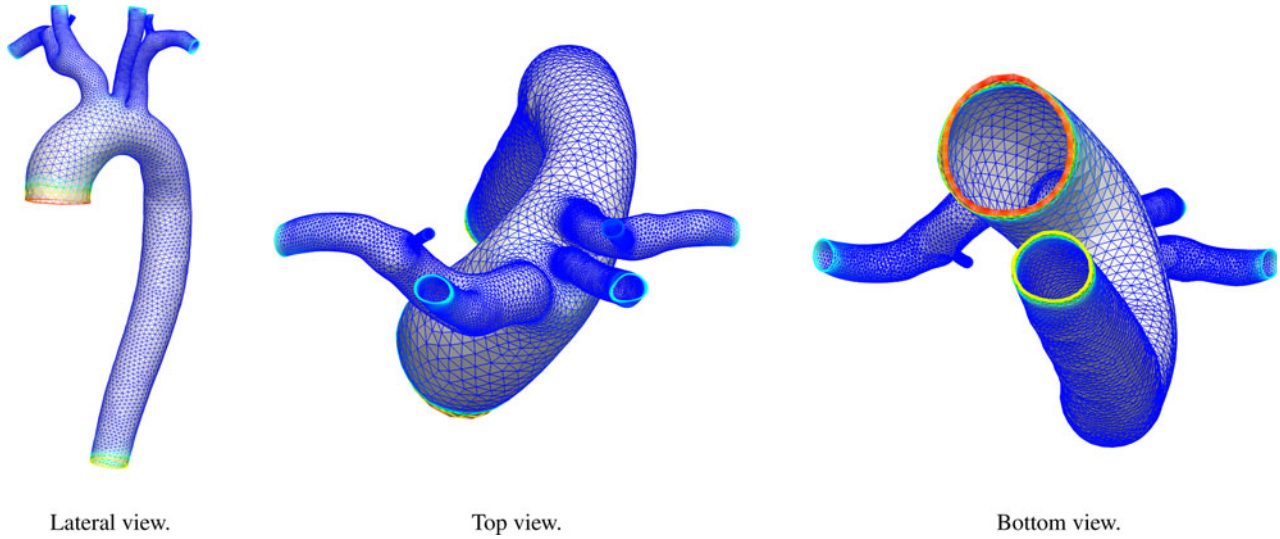


**FIGURE 9. 3-D aorta wall displacement magnitude difference, at the end-systole of the sixth heart beat ($t$ = 4.4 s), between the scaled area and the fixed area cases. The color bar ranges from blue (0.0 cm) to red (0.2 cm).**

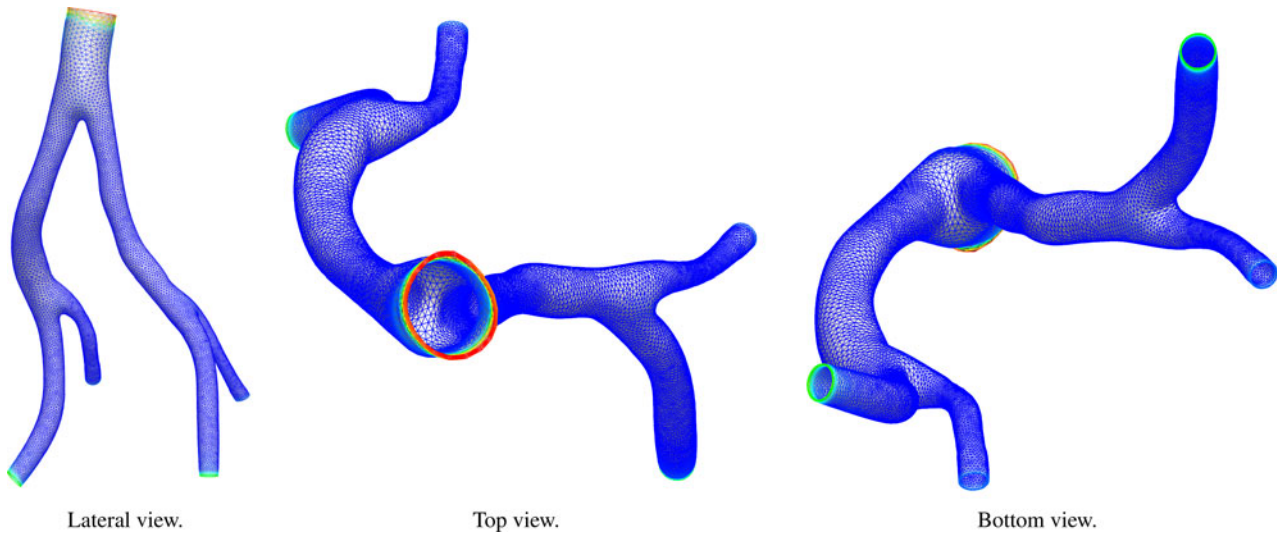


**FIGURE 10. 3-D iliac wall displacement magnitude difference, at the end-systole of the sixth heart beat ($t$ = 4.4 s), between the scaled area and the fixed area cases. The color bar ranges from blue (0.0 cm) to red (0.1 cm).**

case where the same 3-D boundary interfaces are scaled to enforce the continuity of the vessels size with the surrounding 1-D arteries. For these comparisons we use the same geometrical multiscale models introduced in the "External Tissues Parameters Comparisons: 3-D Aorta" and "External Tissues Parameters Comparisons: 3-D Iliac" sections. For the values of the elastic parameter of the external tissues, we select cases $E_4^A$ and $E_{4b}^I$ for the aorta and iliac, respectively, while the viscoelastic parameter is given by (7).

In Figs. 9 and 10 several views of the magnitude difference of the two 3-D geometries displacement fields are shown. In particular, we observe that a significant difference between the two cases exists only near the coupling interfaces, where the boundary conditions change. In the other parts of the wall the result is almost the same. In addition, a further analysis of the flow rate and pressure waveform at the coupling interfaces (which for brevity is not presented here) shows no significant differences between the two

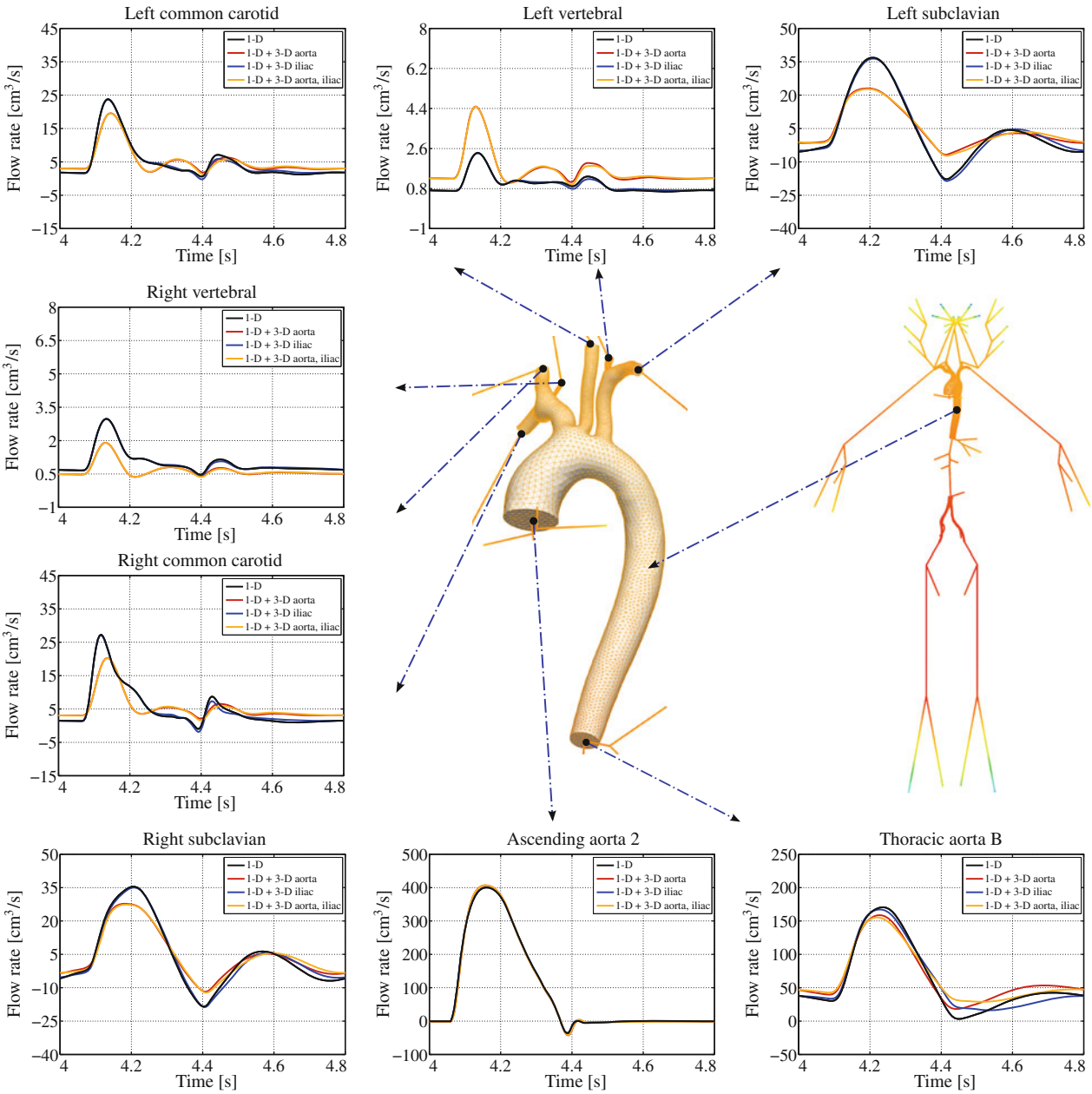


**FIGURE 11. Flow rate comparison, at the sixth heart beat, for different configurations of the global arterial network, at the eight interfaces of the 3-D aorta. The color of the 3-D picture represents the pressure field at the end-systole of the sixth heart beat ($t$ = 4.4 s), where the color bar ranges from blue (80,000 dyn/cm$^2$) to red (165,000 dyn/cm$^2$). Positioning of 1-D network elements is purely visual.**

configurations. This is coherent with the St. Venant–Kirchhoff theory, which states that the influence of the boundary conditions is bounded to the boundaries in dissipative systems. In view of these results we conclude that the continuity of the vessel area between 3-D and 1-D models is not essential for cardiovascular applications, unless the focus of the analysis is on the study of the dynamics and stresses of the wall near the boundary interfaces. On the contrary, it might still be relevant to avoid (or at least reduce) the generation of spurious interface wave reflections in other flow regimes.[37]

### *Geometrical Multiscale Models Comparisons*

In this section we present several comparisons among different geometrical multiscale models. More precisely we compare the results of the full 1-D arterial tree described in the "Human Arterial Tree Model" section, which represents an average healthy patient, with the two dimensionally-heterogeneous models introduced in the "External Tissues Parameters Comparisons: 3-D Aorta" and "External Tissues Parameters Comparisons: 3-D Iliac" sections, and a third model where the 3-D aorta and iliac geometries are coupled together within the same 1-D network. The purpose of the latest model is twofold: on the one hand, it serves to prove the robustness of the presented algorithms in configurations where more than a single 3-D FSI model is included; on the other hand, it is used to analyze the combined effect of multiple disjoint 3-D geometries embedded in the same arterial network, compared to the cases in which just one single 3-D geometry is considered. For all the configurations, we impose the continuity of the vessel area through (6) at the interfaces between the 3-D geometries and the 1-D arteries. Regarding the values of the elastic parameter of the external tissues, we select cases $E_4^A$ and $E_{4b}^I$ for the aorta and iliac, respectively, while the viscoelastic parameter is given by (7).

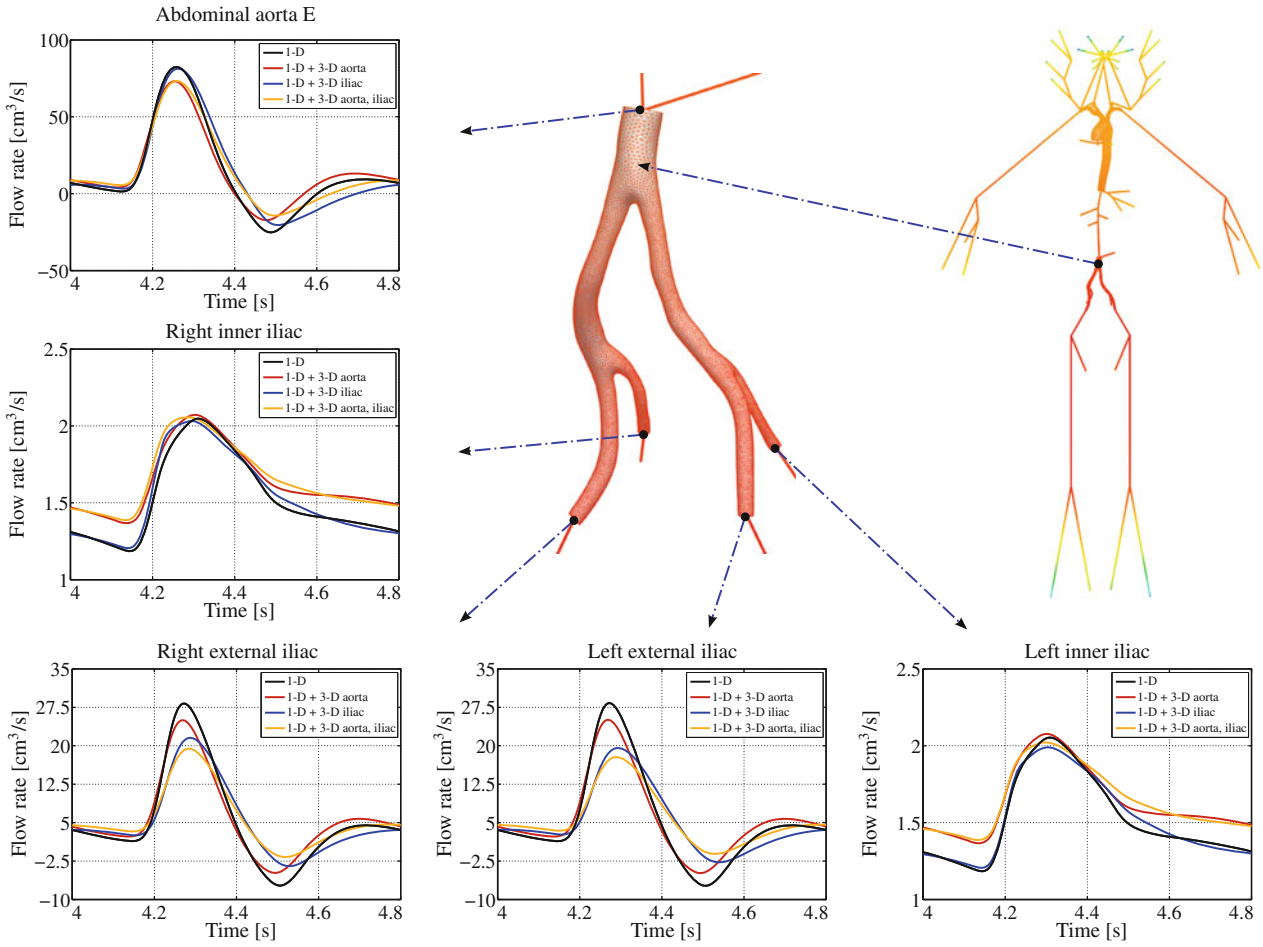


**FIGURE 12. Flow rate comparison, at the sixth heart beat, for different configurations of the global arterial network, at the five interfaces of the 3-D iliac. The color of the 3-D picture represents the pressure field at the end-systole of the sixth heart beat ($t$ = 4.4 s), where the color bar ranges from blue (80,000 dyn/cm$^2$) to red (165,000 dyn/cm$^2$). Positioning of 1-D network elements is purely visual.**

The results of the flow rate waveform comparison at all the coupling interfaces between the 1-D network and the 3-D aorta and iliac are summarized in Figs. 11 and 12, respectively. First of all, we observe that the presence of the 3-D iliac geometry has almost no effect on the upstream solution (apart in the thoracic aorta B interface, which is quite close to the iliac artery), while the 3-D aorta produces a visible, even if small, difference in the downstream flow (see, e.g., the external iliac interfaces). In addition, even if the inlet flow rate is the same in all the cases (see ascending aorta 2 flow rate in Fig. 11) the flow rate at the seven outlets of the aorta is slightly different. This can be justified by observing that the 3-D geometry of the aorta is not symmetric (particularly, the branches have different left and right vessel sizes), thus inducing a different splitting of the flow compared to the one obtained for the full 1-D arterial tree. Particularly, this difference is more pronounced in the vertebral arteries, where the left/right area is equal to 0.1 $cm^2$ in the 1-D network, while in the 3-D geometry we have 0.2 $cm^2$ on the left side and 0.07 $cm^2$ on the right one.

Regarding the behavior of the pressure and, consequently, of the radial scale factor, which are shown in

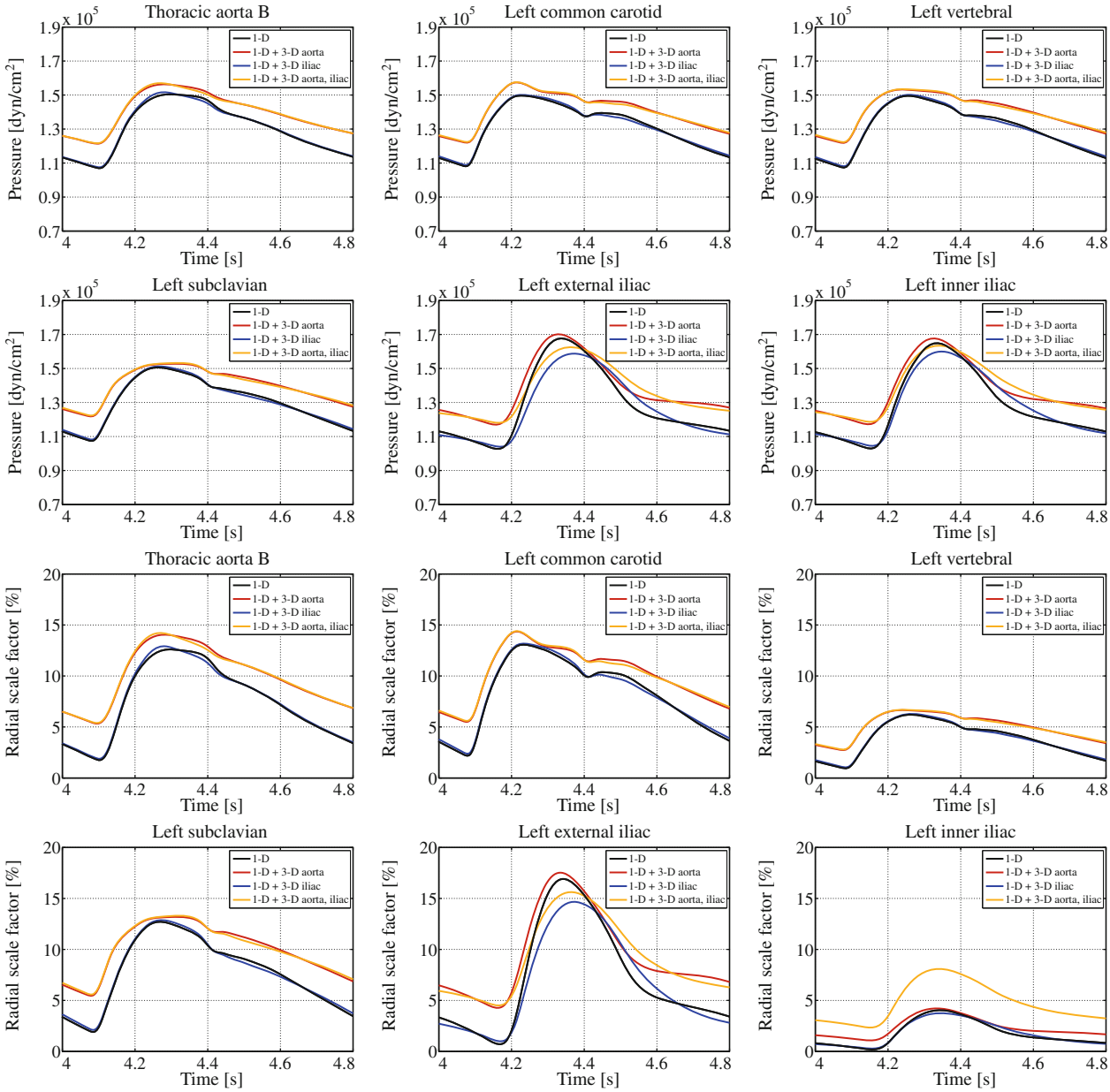


**FIGURE 13. Pressure and radial scale factor comparisons, at the sixth heart beat, for different configurations of the global arterial network, at the most significant coupling interfaces of the 3-D aorta and iliac (see Figs. 11 and 12).**

Fig. 13, we observe a difference in mean values between the cases with and without the 3-D aorta geometry. This is due to an increase in the resistance between the inlet and the outlet, which in turn is due to the presence of 3-D fluid dynamics. This was confirmed by a sensitivity analysis with respect to the Young's modulus (for brevity not reported here), which has shown almost no effect on the level of the end-diastolic pressure. A possible motivation for the increase of the resistance could be related to the presence of the curvature of the aortic arch in the 3-D model, which is not accounted in the 1-D problem. Moreover, recirculation regions as well as friction forces at branching points are also neglected in the 1-D case. In view of these results, we conclude that 3-D patient-specific geometries might have a significant effect on the arterial flow, even in the case of healthy arteries. The presence of geometrical singularities and pathologies, such as aneurysms and stenoses, would probably increase this effect and will make the subject of future works.

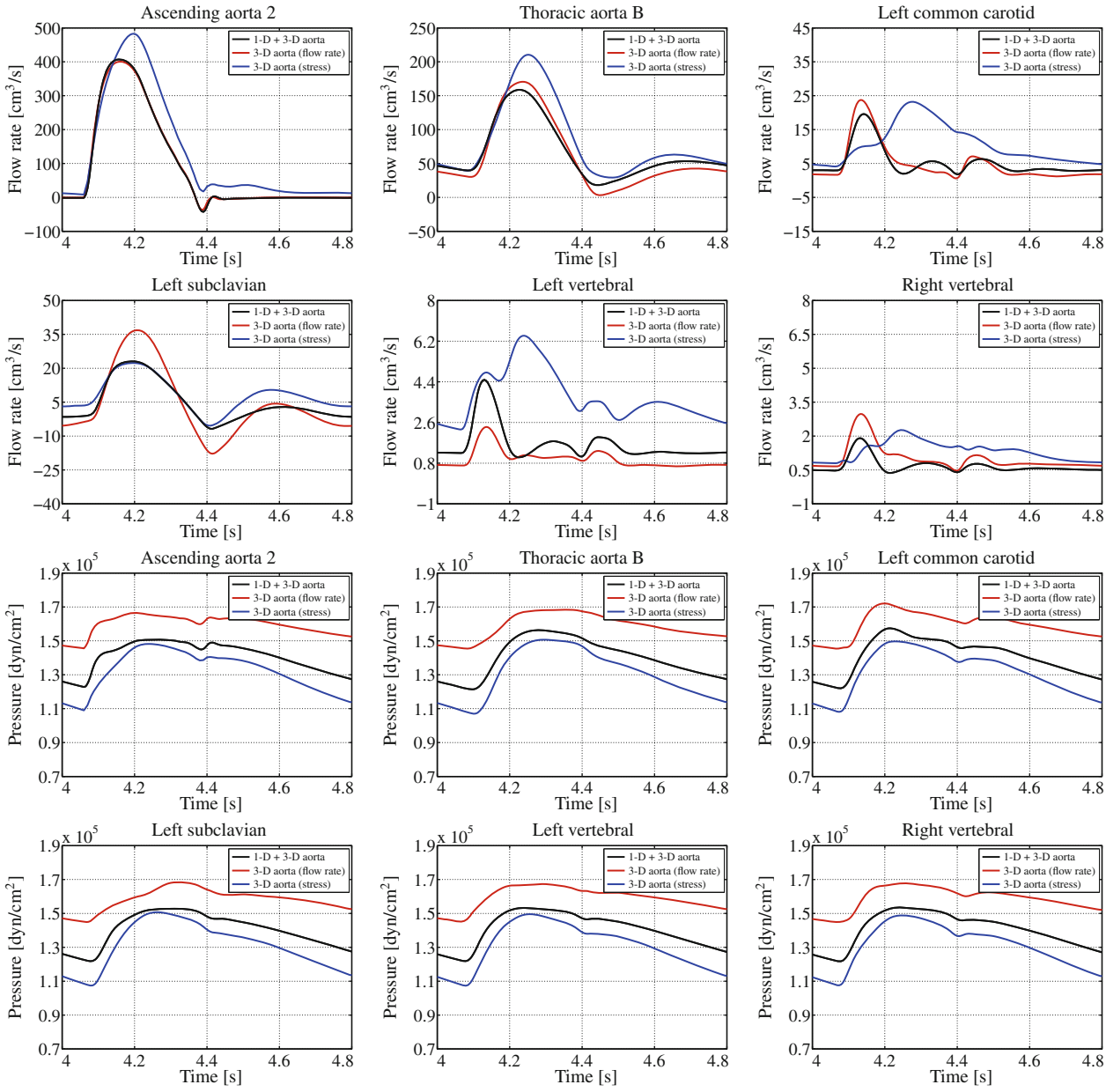


**FIGURE 14. Flow rate and pressure comparisons, at the sixth heart beat, between the solution of the geometrical multiscale problem and the one of the stand-alone 3-D aorta with flow rate or stress boundary data from the full 1-D network, at the most significant coupling interfaces of the 3-D aorta.**

*Stand-Alone 3-D FSI Modeling*

In this section we set up a comparison between the results of the geometrical multiscale models presented in the "External Tissues Parameters Comparisons: 3-D Aorta" and "External Tissues Parameters Comparisons: 3-D Iliac" sections, and their stand-alone 3-D FSI simulations counterparts. More precisely, the stand-alone 3-D problems are set up by considering the same 3-D geometries and data used in the two reference geometrical multiscale models (cases $E_j^0$ and $E_{4b}^I$, respectively, where the viscoelastic parameter is given by (7)). However, at the boundary interfaces, instead of imposing the set of conservation equations with the surrounding models, as described in the "Interface Equations for the Global Network of Models" section we prescribe either flow rate or stress time profiles, taken from a precomputed solution of a full 1-D arterial tree. Following the same approach, we also impose the radial scale factor time profile on the solid ring boundary interfaces, such that they are not fixed.

The flow rate and pressure waveform comparisons, at the most significant coupling interfaces between the 3-D aorta and the 1-D network, are summarized in Fig. 14. The results show significant differences between the reference configuration, i.e., the geometrical multiscale model, and the solution computed by solving the stand-alone 3-D aorta model. For instance, let us consider the flow rate waveform. The red lines coincide with the precomputed (and imposed) solution of the full 1-D arterial tree, which is different from the one of the geometrical multiscale model, as already discussed in the "Geometrical Multiscale Models Comparisons" section. On the contrary, the blue lines are computed by imposing a stress boundary data. However, even in this case, the resulting flow rate is significantly different from the reference one. In particular, the flow rate prediction in the left common carotid and vertebral arteries are clearly incorrect. Regarding the pressure waveform, where the precomputed solution of the full 1-D arterial network coincides with the blue lines, a visible mismatch between the reference solution and the stand-alone cases is always present. In particular, the average pressure level is overestimated when the flow rate is imposed, and underestimated when the stress is prescribed. As a consequence of the different flow rate and pressure waveform, also the displacement field changes, as shown in Fig. 15. The differences with respect to the reference case are more evident when imposing the flow rate, where we also observe a non-physiological excessive strain (overinflation) of the left common carotid artery, even if we use the same values for the tissues parameters in both simulations.

Regarding the stand-alone 3-D iliac model, similar considerations hold, as shown in Figs. 16 and 17. Among other things, we highlight the totally incorrect flow rate prediction in the left inner iliac artery when imposing a stress boundary data.

The results of these comparisons prove the importance of the geometrical multiscale approach in the

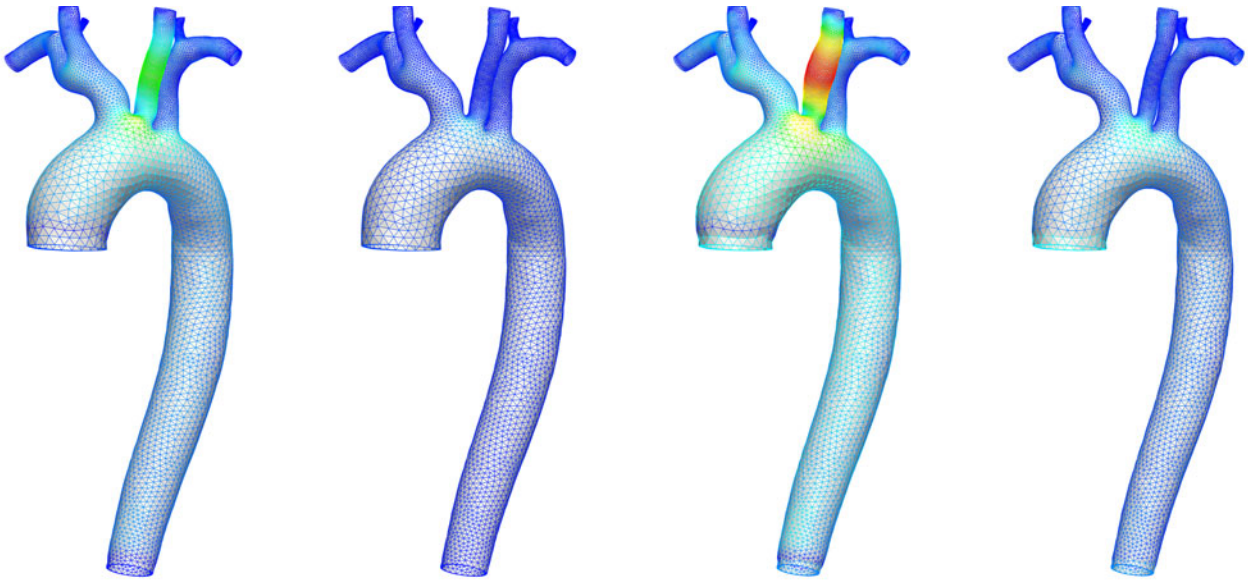


**FIGURE 15. 3-D aorta wall displacement magnitude difference, at the end-systole and end-diastole of the sixth heart beat, between the solution of the geometrical multiscale problem and the one of the stand-alone 3-D aorta with flow rate or stress boundary data from the full 1-D network. The color bar ranges from blue (0.0 cm) to red (0.5 cm).**

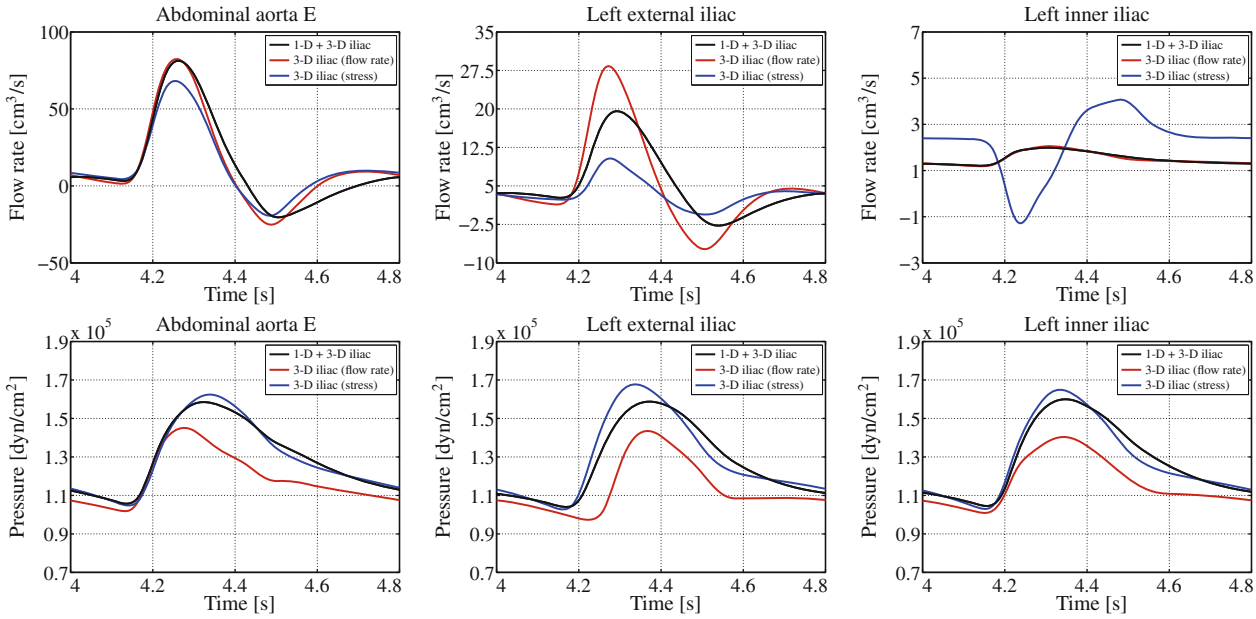


**FIGURE 16. Flow rate and pressure comparisons, at the sixth heart beat, between the solution of the geometrical multiscale problem and the one of the stand-alone 3-D iliac with flow rate or stress boundary data from the full 1-D network, at the most significant coupling interfaces of the 3-D iliac.**

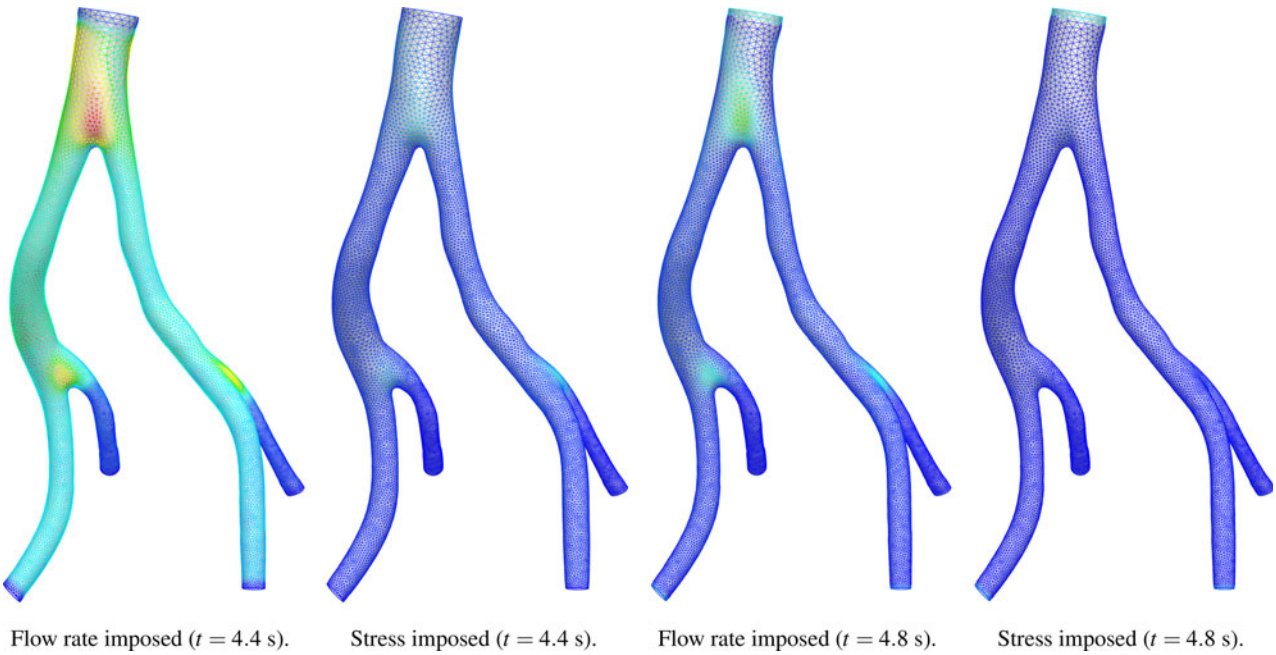


**FIGURE 17. 3-D iliac wall displacement magnitude difference, at the end-systole and end-diastole of the sixth heart beat, between the solution of the geometrical multiscale problem and the one of the stand-alone 3-D iliac with flow rate or stress boundary data from the full 1-D network. The color bar ranges from blue (0.0 cm) to red (0.5 cm).**

modeling of cardiovascular flows. The different behavior of the stand-alone 3-D FSI simulations with respect to the geometrical multiscale model reference cases is mainly due to the lack of dynamic interplay between the dimensionally-heterogeneous models. Indeed, on the one hand, the set of conservation equations described in the "Interface Equations for the Global Network of Models" section provides a reliable and automatic way to determine the boundary data of each coupled model. On the other hand, they also

provide bilateral information on both flow rate and pressure, independently of the imposed boundary condition type.

## CONCLUSIONS

In this work, we presented several numerical comparisons of geometrical multiscale models. A brief description of the main ingredients of the geometrical multiscale approach has been recalled from previous works, together with the partitioned solution strategy used to set up the global network of dimensionally-heterogeneous models.

The purposes of this work were manifold. A first goal was to describe in detail a possible approach to set up and solve geometrical multiscale problems (not only regarding interface equations, network connectivity and solution algorithms, but also with a focus on the set up of the specific problems), and to give more insight on the calibration of the most critical parameters needed by the numerical simulations. In this regard we first provided a short description of the procedure required to plug one or more 3-D patient-specific geometries in a 1-D arterial tree network, whose parameters were calibrated to represent an average healthy patient. Then we set up several comparisons to study the sensitivity of the main quantities of interest (flow rate, pressure, and solid wall displacement) with respect to the elastic and viscoelastic external tissues parameters. These quantities, which appear in the Robin boundary condition on the solid wall of the 3-D FSI models, are empiric coefficients whose evaluation is rather difficult. The results of our analysis show that:

1. the use of purely elastic Robin boundary conditions together with a linear elastic structure might lead to spurious high-frequency oscillations in some arteries, due to the total lack of damping terms in the structural model;
2. viscoelastic Robin boundary conditions can be used to somehow compensate for the lack of damping terms in 3-D FSI model, at least in healthy arteries, where a linear elastic structure can still be considered a reasonable approximation;
3. a simple empiric relation can be used to determine the value of the viscoelastic parameter as a function of the elastic one;
4. above a certain threshold, the sensitivity of the flow rate and pressure waveform to a variation of the external tissues parameters is very small.

In future works, additional investigations will be performed to confirm the results of the first two points. A possible strategy to do this is to try to reproduce the high-frequency oscillations observed in the vertebral arteries by using simpler geometrical configurations, such as a cylindrical benchmark case where the radius, the material properties, and the inflow wave are chosen to be similar to those at the simulated vertebral arteries. In addition, further sets of simulations will be performed on the 3-D geometry of the aorta by varying, for instance, the local thickness of the wall or by including a more accurate model for the structure. Anyway, despite these aspect, we showed that it is possible to estimate, in a systematic way, an admissible range of values for these parameters, such that they lead to reliable physiological results.

Another goal of this work was to prove the importance of the geometrical multiscale approach in the modeling of cardiovascular flows. To do this we compared the results given by geometrical multiscale models with both the solution of a full 1-D arterial tree, and the one of stand-alone 3-D problems, where the 3-D patient-specific geometries were fed with boundary data taken from a precomputed solution of the same full 1-D network. Main results of this analysis are:

1. 3-D patient-specific geometries might produce significant changes in the 1-D arterial flow, even in the case of healthy arteries;
2. flow rate and pressure waveforms produced by stand-alone 3-D FSI simulations are different (and in some cases far) from the ones obtained in comparable geometrical multiscale scenarios: this is due to the fact that stand-alone 3-D FSI simulatons lack the dynamic interplay among the dimensionally-heterogeneous models;
3. the continuity of the vessel area between 3-D and 1-D FSI models is not essential for cardiovascular applications, unless the focus of the analysis is on the study of the dynamics and stresses of the wall near the boundary interfaces.

In summary, despite their increased complexity and computational cost with respect to either 1-D arterial networks or simpler stand-alone 3-D FSI simulations, geometrical multiscale models represent a powerful, accurate tool to study in detail complex cardiovascular problems. Indeed, they give the possibility to detail some specific regions of interest by the mean of 3-D FSI models, evaluating local hemodynamics parameters (e.g., wall shear stress, turbulent flow, regions of recirculation) without neglecting the interaction with the global circulation, accounted through a network of 1-D elements.

## ACKNOWLEDGMENTS

A. C. I. Malossi acknowledges the Swiss Platform for High-Performance and High-Productivity Computing (HP2C). J. Bonnemain acknowledges the Swiss National Fund (SNF) grant 323630-133898. We also acknowledge the European Research Council Advanced Grant "Mathcard, Mathematical Modelling and Simulation of the Cardiovascular System", Project ERC-2008-AdG 227058. Last but not least, we acknowledge Pablo Blanco (LNCC), Simone Deparis (CMCS, EPFL), and Alfio Quarteroni (CMCS, EPFL) for their precious support, as well as Phylippe Reymond (LHTC, EPFL) for the 3-D geometry of the aorta. All the numerical results presented in this paper have been computed using the LifeV library (http://www.lifev.org).

## CONFLICT OF INTEREST

All authors declare that no conflicts of interest exist.

## REFERENCES

[1]Alastruey, J., K. H. Parker, J. Peiró, S. M. Byrd, and S. J. Sherwin. Modelling the circle of Willis to assess the effects of anatomical variations and occlusions on cerebral flows. *J. Biomech.* 40(8):1794–1805, 2007.

[2]Balossino, R., G. Pennati, F. Migliavacca, L. Formaggia, A. Veneziani, M. Tuveri, and G. Dubini. Computational models to predict stenosis growth in carotid arteries: Which is the role of boundary conditions? *Comput. Methods Biomech. Biomed. Eng.* 12(1):113–123, 2009.

[3]Baretta, A., C. Corsini, W. Yang, I. E. Vignon-Clementel, A. L. Marsden, J. A. Feinstein, T.-Y. Hsia, G. Dubini, F. Migliavacca, and G. Pennati. Virtual surgeries in patients with congenital heart disease: a multi-scale modelling test case. *Philos. Trans. R. Soc. Lond. A* 369(1954):4316–4330, 2011.

[4]Bazilevs, Y., V. M. Calo, T. J. R. Hughes, and Y. Zhang. Isogeometric fluid–structure interaction: theory, algorithms, and computations. *Comput. Mech.* 43(1):3–37, 2008.

[5]Bertoglio, C., P. Moireau, and J.-F. Gerbeau. Sequential parameter estimation for fluid-structure problems. Application to hemodynamics. *Int. J. Numer. Methods Biomed. Eng.* 28(4):434–455, 2012.

[6]Blanco, P. J., R. A. Feijóo, and S. A. A. Urquiza. Unified variational approach for coupling 3D–1D models and its blood flow applications. *Comput. Methods Appl. Mech. Eng.* 196(41–44):4391–4410, 2007.

[7]Blanco, P. J., J. S. Leiva , R. A. Feijóo, and G. C. Buscaglia. Black-box decomposition approach for computational hemodynamics: one-dimensional models. *Comput. Methods Appl. Mech. Eng.* 200(13–16):1389–1405, 2011.

[8]Bonnemain, J., A. C. I. Malossi, M. Lesinigo, S. Deparis, A. Quarteroni, and L. K. von Segesser. Numerical simulation of left ventricular assist device implantations: comparing the ascending and the descending aorta cannulations. *Med. Eng. Phys.*, 2013. doi:10.1016/j.medengphy.2013.03.022.

[9]Burman, E., M. A. Fernández, and P. Hansbo. Continuous interior penalty finite element method for Oseen's equations. *SIAM J. Numer. Anal.* 44(3):1248–1274, 2006.

[10]Čanić, S., K. Ravi-Chandar, Z. Krajcer, D. Mirković, and S. Lapin. Mathematical model analysis of Wallstent® and AneuRx®: dynamic responses of bare-metal endoprosthesis compared with those of stent-graft. *Tex. Heart Inst. J.* 34(4):502–506, 2005.

[11]Crosetto, P. Fluid–Structure Interaction Problems in Hemodynamics: Parallel Solvers, Preconditioners, and Applications. PhD thesis, École Polytechnique Fédérale de Lausanne, 2011. http://infoscience.epfl.ch/record/166924.

[12]Crosetto, P., S. Deparis, L. Formaggia, G. Mengaldo, F. Nobile, and P. A. Tricerri. A comparative study of different nonlinear hyperelastic isotropic arterial wall models in patient-specific vascular flow simulations in the aortic arch. Submitted, 2012.

[13]Crosetto, P., S. Deparis, G. Fourestey, and A. Quarteroni. Parallel algorithms for fluid-structure interaction problems in haemodynamics. *SIAM J. Sci. Comput.* 33(4):1598–1622, 2011a.

[14]Crosetto, P., P. Reymond, S. Deparis, D. Kontaxakis, N. Stergiopulos, and A. Quarteroni. Fluid–structure interaction simulation of aortic blood flow. *Comput. Fluids* 43(1):46–57, 2011b.

[15]D'Elia, M., and A. Veneziani. Uncertainty quantification for data assimilation in a steady incompressible Navier–Stokes problem. *ESAIM Math. Model. Numer. Anal.* 2013. doi:10.1051/m2an/2012056.

[16]Euler, L. Principia pro motu sanguinis per arterias determinando (1775). *Opera Posthuma Mathematica et Physica* 2:814–823, 1844.

[17]Faggiano, E., J. Bonnemain, A. Quarteroni, and S. Deparis. A patient-specific framework for the analysis of the haemodynamics in patients with ventricular assist device. Submitted, 2012.

[18]Figueroa, C. A., S. Baek, C. A. Taylor, and J. D. Humphrey. A computational framework for fluid-solid-growth modeling in cardiovascular simulations. *Comput. Methods Appl. Mech. Eng.* 198(45–463):3583–3601, 2009.

[19]Formaggia, L., D. Lamponi, and A. Quarteroni. One-dimensional models for blood flow in arteries. *J. Eng. Math.* 47(3–4):251–276, 2003.

[20]Formaggia, L., A. Moura, and F. Nobile. On the stability of the coupling of 3D and 1D fluid–structure interaction models for blood flow simulations. *ESAIM Math. Model. Numer. Anal.* 41(4):743–769, 2007.

[21]Formaggia, L., F. Nobile, A. Quarteroni, and A. Veneziani. Multiscale modelling of the circulatory system: a preliminary analysis. *Comput. Vis. Sci.* 2(2–3):75–83, 1999.

[22]Formaggia, L., A. Quarteroni, and A. Veneziani. Cardiovascular Mathematics, Vol. 1 of Modeling, Simulation & Applications. Milan: Springer, 2009.

[23]Formaggia, L., A. Veneziani, and C. Vergara. Flow rate boundary problems for an incompressible fluid in deformable domains: formulations and solution methods. *Comput. Methods Appl. Mech. Eng.* 199(9–12):677–688, 2010.

[24]Fung, Y. C. Biomechanics: Mechanical Properties of Living Tissues, 2nd ed. New York: Springer, 1993.

[25]Gerbeau, J.-F., M. Vidrascu, and P. Frey. Fluid–structure interaction in blood flows on geometries based on medical imaging. *Comput. Struct.* 83(2–3):155–165, 2005.

[26]Grinberg, L., T. Anor, J. R. Madsen, A. Yakhot, and G. E. Karniadakis. Large-scale simulation of the human arterial tree. *Clin. Exp. Pharmacol. Physiol.* 36(2):194–205, 2009.

[27]Holzapfel, G. A., and R. W. Ogden. Mechanics of Biological Tissue. Berlin: Springer, 2006.
[28]Holzapfel, G. A., T. C. Gasser, and R. W. Ogden. A new constitutive framework for arterial wall mechanics and a comparative study of material models. *J. Elasticity* 61(1–3):1–48, 2000.
[29]Kanyanta, V., A. Ivankovic, and A. Karac. Validation of a fluid–structure interaction numerical model for predicting flow transients in arteries. *J. Biomech.* 42(11):1705–1712, 2009.
[30]Laganàà, K., G. Dubini, F. Migliavacca, R. Pietrabissa, G. Pennati, A. Veneziani, and A. Quarteroni. Multiscale modelling as a tool to prescribe realistic boundary conditions for the study of surgical procedures. *Biorheology* 39(3):359–364, 2002.
[31]Langewouters, G. J. Visco-Elasticity of the Human Aorta In Vitro in Relation to Pressure and Age. PhD thesis, Free University, Amsterdam, 1982.
[32]Li, D., and A. M. Robertson. A Structural multi-mechanism damage model for cerebral arterial tissue. *J. Biomech. Eng.* 131(10):101013 (8 pages), 2009.
[33]Liu, Y., C. Dang, M. Garcia, H. Gregersen, and G. S. Kassab. Surrounding tissues affect the passive mechanics of the vessel wall: theory and experiment. *Am. J. Physiol. Heart Circ. Physiol.* 293(6):H3290–H3300, 2007.
[34]Malossi, A. C. I. Partitioned Solution of Geometrical Multiscale Problems for the Cardiovascular System: Models, Algorithms, and Applications. PhD thesis, École Polytechnique Fédérale de Lausanne, 2012. http://infoscience.epfl.ch/record/180639.
[35]Malossi, A. C. I., P. J. Blanco, S. Deparis, and A. Quarteroni. Algorithms for the partitioned solution of weakly coupled fluid models for cardiovascular flows. *Int. J. Numer. Methods Biomed. Eng.* 27(12):2035–2057, 2011.
[36]Malossi, A. C. I., P. J. Blanco, and S. Deparis. A two-level time step technique for the partitioned solution of one-dimensional arterial networks. *Comput. Methods Appl. Mech. Eng.* 237–240:212–226, 2012.
[37]Malossi, A. C. I., P. J. Blanco, P. Crosetto, S. Deparis, and A. Quarteroni. Implicit coupling of one-dimensional and three-dimensional blood flow models with compliant vessels. *SIAM J. Multiscale Model. Simul.* 11(2):474–506, 2013.
[38]Martin, V., F. Clément, A. Decoene, and J.-F. Gerbeau. Parameter identification for a one-dimensional blood flow model. In: Proceedings of the CEMRACS: Mathematics and Applications to Biology and Medicine, Vol. 14. EAIM, 2005, pp. 174–200.
[39]Moireau, P., N. Xiao, M. Astorino, C. A. Figueroa, D. Chapelle, C.-A. Taylor, and J.-F. Gerbeau. External tissue support and fluid–structure simulation in blood flows. *Biomech. Model. Mechanobiol.* 11(1–2):1–18, 2012.
[40]Papadakis, G. Coupling 3D and 1D fluid–structure-interaction models for wave propagation in flexible vessels using a finite volume pressure-correction scheme. *Commun. Numer. Methods Eng.* 25(5):533–551, 2009.
[41]Passerini, T., M. de Luca, L. Formaggia, A. Quarteroni, A. Veneziani. A 3D/1D geometrical multiscale model of cerebral vasculature. *J. Eng. Math.* 64(4):319–330, 2009.
[42]Reymond, P., Y. Bohraus, F. Perren, F. Lazeyras, N. Stergiopulos. Validation of a patient-specific one-dimensional model of the systemic arterial tree. *Am. J. Physiol. Heart Circ. Physiol.* 301(3):H1173–H1182, 2011.
[43]Reymond, P., F. Merenda, F. Perren, D. Rüfenacht, N. Stergiopulos. Validation of a one-dimensional model of the systemic arterial tree. *Am. J. Physiol. Heart Circ. Physiol.* 297(1):H208–H222, 2009.
[44]Robertson, A. M., M. R. Hill, and D. Li. Structurally motivated damage models for arterial walls. Theory and application. In: Modeling of Physiological Flows, Vol. 5 of Modeling, Simulation & Applications. Milan: Springer, 2011, pp. 143–185.
[45]Shi, Y., P. Lawford, and R. Hose. Review of Zero-D and 1-D models of blood flow in the cardiovascular system. *BioMed. Eng. OnLine* 10(33):1–38, 2011.
[46]Tezduyar, T. E., and S. Sathe. Modeling of fluid–structure interactions with the space–time finite elements: solution techniques. *Int. J. Numer. Methods Fluids* 54(6–8):855–900, 2006.
[47]Vignon-Clementel, I. E., C. A. Figueroa, K. E. Jansen, and C. A. Taylor. Outflow boundary conditions for three-dimensional finite element modeling of blood flow and pressure in arteries. *Comput. Methods Appl. Mech. Eng.* 195(29–32):3776–3796, 2006.
[48]Xiao, N., J. D. Humphrey, and C. A. Figueroa. Multi-scale computational model of three-dimensional hemodynamics within a deformable full-body arterial network. *J. Comput. Phys.*, 2013.